J. Fluid Mech. (1991), *vol.* 222, *pp.* 157–196
Printed in Great Britain

A numerical study of oscillating flow around a circular cylinder

By PETER JUSTESEN

Institute of Hydrodynamics and Hydraulic Engineering, Technical University of Denmark, DK-2800 Lyngby, Denmark

(Received 5 September 1989 and in revised form 28 May 1990)

This paper presents results obtained from a numerical solution to a stream function–vorticity formulation of the Navier–Stokes equations for the flow around a circular cylinder in planar oscillating flow at small Keulegan–Carpenter numbers (KC) in the subcritical Reynolds number (Re) range. The equations are solved by finite-difference methods. For very small KC ($\leqslant 1$), the numerical results coincide with analytical solutions. As KC is increased, the incipient separation and instability leading to an asymmetrical flow with vortex shedding are predicted. Computed flow fields at small KC values are compared to flow visualizations, and good agreement is found for moderate β-values (≈ 250). The well-documented flow regimes with the transverse vortex street, single-, double- and three-pair shedding, are predicted by the model. Although the flow is not fully resolved for the highest Re values, comparisons of calculated drag and inertia coefficients with experimental data for three different values of the frequency parameter β in the range 196–1035 for $0 < KC < 26$ show good agreement.

1. Introduction

The classical fluid mechanics problem of flow around a circular cylinder in a steady flow has been studied extensively using numerical methods. This paper addresses the situation in which the ambient flow is a planar oscillatory flow with a high frequency such that the Keulegan–Carpenter number (KC) is small. KC is defined by

$$KC = \frac{U_m T}{D}, \tag{1a}$$

where D is the cylinder diameter, U_m the velocity amplitude, and T is the period of oscillation. The associated Reynolds number is

$$Re = \frac{U_m D}{\nu}, \tag{1b}$$

ν being the kinematic viscosity of the fluid, and the frequency parameter, β, is given by

$$\beta = \frac{Re}{KC} = \frac{D^2}{\nu T}. \tag{1c}$$

In practice, this problem has interest in connection with hydrodynamic forces on, and damping of, large cylindrical elements in offshore structures subjected to the action of waves. When KC is small, the member is mainly subjected to inertia forces, but the drag force determines the hydrodynamic damping of flexible structures.

Hence, the drag force is very important, even though it is insignificant as a direct force acting on a fixed structure, since it will control the vibration amplitude. As KC increases, the drag force will also become important as a direct force. At $KC \approx 20$ the inertia and drag forces are equal in magnitude.

Under real conditions, the structural members may be covered by marine fouling and the flow velocities will be high such that the flow is turbulent. In this study, only subcritical flow will be considered. The prediction of turbulent flow will be dependent on the construction of a suitable turbulence model and is beyond the scope of the present paper.

Most numerical studies of the steady flow past a circular cylinder have dealt with the problem in two dimensions owing to the limitations in available computer resources. Notwithstanding the fact that this flow is highly three-dimensional even at low Reynolds numbers (Williamson 1989), considerable insight has been gained from the two-dimensional simulations. In analogy, the present two-dimensional flows around a circular cylinder in oscillating flow are unlikely to be realizable, but they do exhibit many of the important intrinsic features found in the similar three-dimensional flow and are therefore considered worth computing.

The flow at very small KC has been studied analytically first by Stokes (1851) and then by Wang (1968) who developed an asymptotic theory assuming that the flow remains attached. It is well established, however, that as KC is increased, the flow will separate and eventually become asymmetrical (Sarpkaya 1986 and Bearman *et al.* 1985). Honji (1981) made flow visualizations which showed that a three-dimensional instability develops at small KC. This instability is probably important for the drag forces (Sarpkaya 1986), which means that two-dimensional calculations cannot be expected to conform with the experiments when the Honji instability is present.

Experimental investigations of the oscillatory flow around a circular cylinder at small KC have shown that the flow can be classified into a number of different flow regimes governed mainly by KC and with a weak dependency on Re (Bearman *et al.* 1981; Williamson 1985; Sarpkaya 1986). At $KC \ll 1$, the flow remains symmetrical, attached, and two-dimensional. As KC is increased from ≈ 0, the flow will become asymmetrical at $KC \approx 2$–3. After that the flow will pass through (in the KC sense) a number of well-defined vortex shedding patterns corresponding to an increasing number of vortices being shed in each cycle of oscillation.

A few attempts have been made to study the present two-dimensional flow by Eulerian finite-difference solutions to the Navier–Stokes equations using the primitive variables. Baba & Miyata (1987) have presented two calculations for $KC = 5$ and 7 at $Re \approx 10^3$. Although physically unrealistic, the flow was symmetric in both simulations. Murashige, Hinatsu & Kinoshita (1989) have used a similar method to analyse three cases ($KC = 5$, 7 and 10) at the higher Re value of around 10^4. The flow was perturbed by artificial means to trigger an asymmetry. At $KC = 10$, a transverse vortex street appeared, in agreement with experimental observations by for example Williamson (1985).

Mixed Eulerian–Lagrangian discrete-vortex methods have been used by Stansby & Smith (1989), Graham & Djahansouzi (1989), and Skomedal, Vada & Sortland (1989) to compute the two-dimensional flow. The two first studies concentrated on the region $0 < KC < 6$. Calculated force efficients in the Morison equation have been found to compare well with experimental data. Skomedal *et al.* did calculations up to $KC = 22.5$. Furthermore they considered a single cylinder as well as a two-cylinder

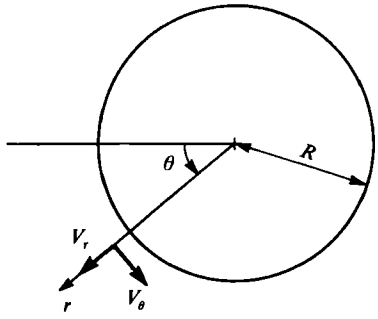

FIGURE 1. Definition sketch.

configuration. Again good agreement between measured and calculated forces was observed.

This paper presents solutions to the stream function–vorticity formulation of the Navier–Stokes equations obtained by an Eulerian finite-difference method. In addition to providing new insight into the flow, this study is also complementary to the previous studies made using the finite-difference methods as well as the vortex methods.

Emphasis is placed on the analysis of subcritical flows in the region for which $KC < 26$. It is assumed that the boundary layers remain laminar. This assumption is valid at least for the smaller KC, whereas the present calculations are not fully resolved for the highest values of Re (and thus KC). The results are, however, very useful for the understanding of the physics of the flow. The numerical results will be checked against flow visualizations and force measurements. When possible, a comparison will be made with alternative numerical solutions as well.

The issues of separation inception and onset of asymmetrical flow are addressed first. Then the symmetrical flow regime at very small KC is discussed. Finally, the results in the asymmetrical flow regimes at larger values of KC are presented.

2. Theory

2.1. *The equations*

Consider a two-dimensional flow field which is described in a polar coordinate system. The geometry is depicted in figure 1. The velocities in the r^*- and θ-directions are denoted V_r^* and V_θ^*, respectively. A stream function, ψ^*, is defined by the relations

$$V_r^* = \frac{1}{r^*}\frac{\partial \psi^*}{\partial \theta}, \quad V_\theta^* = -\frac{\partial \psi^*}{\partial r^*}. \tag{2}$$

The vorticity is defined as

$$\omega^* = \frac{1}{r^*}\left(\frac{\partial}{\partial r^*}(r^* V_\theta^*) - \frac{\partial V_r^*}{\partial \theta}\right). \tag{3}$$

By cross-differentiation of the Navier–Stokes equations, thus eliminating the pressure from the equations, the vorticity transport equation is obtained:

$$\frac{\partial \omega^*}{\partial t^*} + \frac{1}{r^*}\frac{\partial}{\partial r^*}(r^* V_r^* \omega^*) + \frac{1}{r^*}\frac{\partial}{\partial \theta}(V_\theta^* \omega^*) = \nu\left[\frac{1}{r^*}\frac{\partial}{\partial r^*}\left(r^* \frac{\partial \omega^*}{\partial r^*}\right) + \frac{1}{r^{*2}}\frac{\partial^2 \omega^*}{\partial \theta^2}\right], \tag{4}$$

in which ν is the kinematic viscosity of the fluid. When the velocities are expressed as derivatives of the stream function, the continuity equation appears as a Poisson equation for ψ^*.

$$\frac{\partial^2\psi^*}{\partial r^{*2}}+\frac{1}{r^*}\frac{\partial\psi^*}{\partial r^*}+\frac{1}{r^{*2}}\frac{\partial^2\psi^*}{\partial\theta^2}=-\omega^*. \tag{5}$$

In order to examine cases with an unsteady external flow field, it is convenient to separate the stream function into two parts:

$$\psi^*=\psi^*_{\mathrm{p}}+\psi^*_{\mathrm{v}}. \tag{6}$$

ψ^*_{p} is the stream function due to some prescribed externally driven potential flow field (e.g. oscillatory motion) and it satisfies by definition the homogeneous version of (5), i.e. the Laplace equation. ψ^*_{v} is the stream function which may be interpreted as a correction to ψ^*_{p} due to the viscosity of the fluid. ψ^*_{p} has to satisfy the Poisson equation (5).

The following dimensionless variables are introduced:

$$r=\frac{r^*}{R},\quad t=\frac{t^*U_{\mathrm{m}}}{R},\quad V_r=\frac{V^*_r}{U_{\mathrm{m}}},\quad V_\theta=\frac{V^*_\theta}{U_{\mathrm{m}}},\quad \omega=\frac{R\omega^*}{U_{\mathrm{m}}},\quad \psi=\frac{\psi^*}{U_{\mathrm{m}}}, \tag{7}$$

where R is the cylinder radius.

The r-coordinate is strained using a logarithmic transformation in order to resolve the large gradients near the cylinder surface. The equations will then be formulated in a (z,θ) log-polar coordinate system in which z is given by

$$r=\mathrm{e}^z-a \tag{8}$$

and a is a straining parameter. For $a=0$, this transformation defaults to the logarithmic straining used by Braza, Chassaing & Ha Minh (1986) and Borthwick (1986). The introduction of the constant a makes it possible to have a denser distribution of computational points close to the cylinder surface without increasing the total number of grid points. Recently Stansby & Smith (1989) has used a similar transformation.

The governing equations then read

$$A(z)\frac{\partial\omega}{\partial t}+\frac{\partial\psi}{\partial\theta}\frac{\partial\omega}{\partial z}-\frac{\partial\psi}{\partial z}\frac{\partial\omega}{\partial\theta}=\frac{2}{Re}\left[C(z)\frac{\partial^2\omega}{\partial z^2}+B(z)\frac{\partial\omega}{\partial z}+\frac{1}{C(z)}\frac{\partial^2\omega}{\partial\theta^2}\right], \tag{9}$$

$$C(z)\frac{\partial^2\psi_{\mathrm{v}}}{\partial z^2}+B(z)\frac{\partial\psi_{\mathrm{v}}}{\partial z}+\frac{1}{C(z)}\frac{\partial^2\psi_{\mathrm{v}}}{\partial\theta^2}=-A(z)\omega, \tag{10}$$

$$A(z)=\mathrm{e}^z(\mathrm{e}^z-a),\quad B(z)=\frac{a}{\mathrm{e}^z},\quad C(z)=\frac{\mathrm{e}^z-a}{\mathrm{e}^z}. \tag{11a–c}$$

The dimensionless velocities are given by

$$V_r=\frac{1}{\mathrm{e}^z-a}\frac{\partial\psi}{\partial\theta} \tag{12}$$

and

$$V_\theta=-\frac{1}{\mathrm{e}^z}\frac{\partial\psi}{\partial z}. \tag{13}$$

2.2. *Boundary and initial conditions*

The computational domain will be the area bounded by the cylinder surface and a circular boundary at $z = z_\infty$. The boundary conditions at the outer boundary of that area are chosen as

$$\frac{\partial \omega}{\partial z}(z_\infty, \theta, t) = 0, \quad \frac{\partial \psi_v}{\partial z}(z_\infty, \theta, t) = 0. \tag{14}$$

The proper formulation of these boundary conditions has been subject to many discussions in the literature. A careful choice of boundary conditions is a prerequisite for the numerical model to give useful results. The present problem is that an unbounded domain must be approximated by a finite computational domain. Some researchers have used (14) inside the wake region and matched to the Oseen solution outside the downstream wake. This procedure may not be applicable to oscillatory flow in which the wake is not confined to an area downstream. Borthwick (1986) has compared the two conditions and found practically no difference provided that z_∞ is about $80R$ or more. The present study is concerned with oscillatory flow, in which case the generated vorticity will remain within a limited distance from the cylinder, and thus the problem of the outer boundary is assumed not to be critical.

The boundary condition for ψ_v on the cylinder surface is derived from the no-slip and impermeability conditions such that

$$\psi_v(z_0, \theta, t) = V_r(z_0, \theta, t) = V_\theta(z_0, \theta, t) = 0 \tag{15}$$

z_0 is the cylinder surface coordinate. The corresponding condition for ω is obtained by writing the stream-function equation (10) on the cylinder surface:

$$\omega(z_0, \theta, t) = -\frac{C(z)}{A(z)} \frac{\partial^2 \psi}{\partial z^2}\bigg|_{z=z_0} - \frac{B(z)}{A(z)} \frac{\partial \psi}{\partial z}\bigg|_{z=z_0}. \tag{16}$$

The initial conditions for a time-dependent problem are those of a potential flow field. This means that initially at $t = t_0$ the vorticity and the stream function ψ_v are zero everywhere, and the stream function ψ_p takes its well-known solution

$$\psi_p(z, \theta, t_0) = -(e^z - a)\left(1 - \frac{1}{(e^z - a)^2}\right) \sin(\theta) U_\infty(t_0). \tag{17}$$

The free-stream velocity $U_\infty(t)$ is dependent only on time. It takes the value of unity for a uniform flow case. In oscillatory flow U_∞ is

$$U_\infty(t) = \sin(\pi t / KC). \tag{18}$$

It is convenient to introduce the phase angle $\phi = \pi t / KC$. We shall refer to this angle in radians or degrees.

3. The numerical method

In the numerical solution, (9) and (10) are assumed to be decoupled. Each equation is solved once every time step as the solution is advanced in time. We only have to solve the equation for ψ_v, since the solution for ψ_p is known *a priori*.

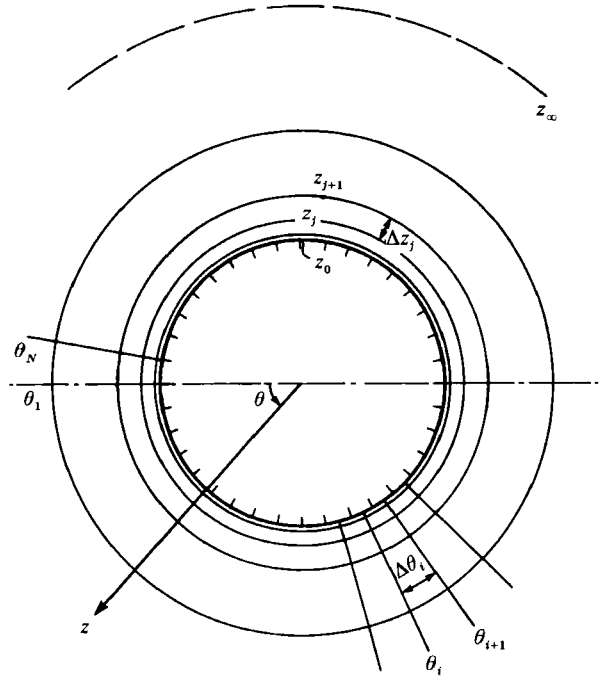

FIGURE 2. Finite-difference mesh. N points in the θ-direction and M points in the z-direction.

3.1. *The vorticity transport equation*

The vorticity transport equation is discretized in space in the finite-difference grid depicted in figure 2. An ADI method which decouples the z- and θ-directions is employed. Borthwick (1986) described the method in detail when using central differencing on all terms including the advective terms. In the present study it was found that this approach often leads to the well-known instabilities at the highest resolvable wavenumbers. Such instabilities can be avoided by introducing the hybrid scheme (see Patankar 1980) in which an upwind differencing is used for the advective terms when advection is dominating over diffusion, i.e. when the Péclet number or cell Reynolds number, defined as

$$Pe = \frac{U\Delta x}{\nu}, \tag{19}$$

is larger than a prescribed value. Δx is the grid spacing, and U is the local velocity. According to Patankar, $Pe \geqslant 2$ is a reasonable choice. When $Pe < 2$, central differencing is used. For details about the ADI method, see Borthwick (1986). The extension to the present hybrid scheme is straightforward.

As argued by Leonard (1979) this could be a questionable approach. The dampening of the instabilities at the highest wavenumbers in the hybrid scheme is due to the artificial or numerical viscosity inherent in the scheme. Therefore we shall examine the possible effects of the numerical viscosity on the results by successive grid refinement in §6.2.1.

3.2. *The stream-function equation*

A Fourier series method is employed for the Poisson equation for ψ_v. Assume that ψ_v and ω can be expressed as Fourier series in the θ-direction:

$$\psi_v(z,\theta) = \tfrac{1}{2}a_0 + \sum_{k=1}^{N/2-1} [a_k \cos(k\theta) + b_k \sin(k\theta)] + a_{N/2}\cos(\tfrac{1}{2}N\theta), \tag{20a}$$

$$\omega(z,\theta) = \tfrac{1}{2}c_0 + \sum_{k=1}^{N/2-1} [c_k \cos(k\theta) + d_k \sin(k\theta)] + c_{N/2}\cos(\tfrac{1}{2}N\theta). \tag{20b}$$

The component $k = \frac{1}{2}N$ corresponds to the highest resolvable wavenumber in the grid. $(a_k(z), b_k(z))$ and $(c_k(z), d_k(z))$ are the Fourier coefficients for ψ_v and ω, respectively. They are a function of z. k is the wave (or mode) number.

The coefficients $(c_k(z), d_k(z))$ can be found from the known ω-field by a forward FFT transformation. Substituting (20) into (10) and using orthogonality relations, one can obtain N ordinary differential equations for the N Fourier coefficients $(a_k(z), b_k(z))$:

$$C(z)\frac{d^2a_k}{dz^2} + B(z)\frac{da_k}{dz} - \frac{1}{C(z)}k^2a_k = -A(z)\,c_k; \quad k = 0,\ldots,\tfrac{1}{2}N, \tag{21a}$$

$$C(z)\frac{d^2b_k}{dz^2} + B(z)\frac{db_k}{dz} - \frac{1}{C(z)}k^2b_k = -A(z)\,d_k; \quad k = 1,\ldots,\tfrac{1}{2}N-1. \tag{21b}$$

Owing to the transformation given by (8) it is not possible to use Fourier transforms in the z-direction. Instead, the N equations are discretized in the z-direction using second-order-accurate central differences. This leads to a system of linear equations for each mode. Inversion of the tridiagonal matrices is performed efficiently using the double-sweep algorithm.

When the Fourier coefficients have been determined, the new ψ_v-field is obtained by inverse Fourier transformation. To obtain the total ψ, the appropriate ψ_p given by (17) is added to ψ_v.

3.3. *Calculation of pressure and forces*

The pressure is not calculated explicitly in the ψ–ω formulation, but has to be found by integration of the momentum equations. Only the surface pressure is of interest in the present paper because it enters the force calculation. The tangential momentum equation written for the cylinder surface can be reduced to

$$\frac{\partial p}{\partial \theta} = \frac{2}{Re}\frac{1}{e^z}\frac{\partial \omega}{\partial z}. \tag{22}$$

The pressure is made dimensionless by ρU_m^2. Integration of (22) is carried out as described by Borthwick (1986). The result is the surface pressure distribution, apart from an arbitrary reference constant. Surface stresses are determined from the equation

$$\tau_w = \frac{\tau_w^*}{\rho U_m^2} = \frac{2}{Re}\omega(z_0) \tag{23}$$

The instantaneous dimensionless (by $0.5\rho DU_m^2$) in-line and transverse force components can now be found by integration:

$$F_x = \int_0^{2\pi} p\cos\theta\,\mathrm{d}\theta + \frac{2}{Re}\int_0^{2\pi} \omega\sin\theta\,\mathrm{d}\theta, \tag{24a}$$

$$F_y = \int_0^{2\pi} p\sin\theta\,\mathrm{d}\theta - \frac{2}{Re}\int_0^{2\pi} \omega\cos\theta\,\mathrm{d}\theta. \tag{24b}$$

Notice that the pressure and friction parts of the forces can be found separately. When the flow is symmetric, F_y vanishes by definition.

3.4. *Implementation*

Initially the code was implemented on an Amdahl VP1100 in vectorized Fortran, but it was later transferred to an IBM PS/2 model 70-121 using Fortran under OS/2. The majority of the results given in this paper has been obtained on this machine.

4. Flow-visualization experimental method

Flow visualizations were conducted in a water tank with a working section 0.8 m high and 0.6 m wide. The model cylinder was mounted vertically from a horizontal Perspex plate which was supported by a horizontal carriage system resting on the tank walls. The oscillatory flow was created by driving the carriage in the horizontal direction thereby oscillating the cylinder in the otherwise still water.

The carriage was driven by a steel bar eccentrically attached to a flywheel which in turn was driven by an electric motor via a short strap. The carriage could attain oscillation amplitudes of $0.032 \leqslant a \leqslant 0.048$ m.

The so-called aluminium powder technique was used to visualize the water movements. The water surface was illuminated by light sources around the tank and photographed using a Nikon motordrive camera at regular, preset time intervals using a special timing device developed by the Danish Hydraulic Institute. For the pictures shown in this paper, the camera was fixed to the carriage such that the cylinder would remain stationary in the picture frame of reference. This allowed for a good representation of the boundary layers and the flow near the cylinder at the expense of reducing the far-field flow to essentially being the ambient flow.

Two cylinders with diameters 0.090 m and 0.050 m were used for $KC = 2.2$ and $KC = 4.0$, respectively. In both cases, β was 250.

5. Initial validation of the model

In order to check the implementation of the mathematical model on the computer, an initial study of impulsively started flow around a circular cylinder was carried out. The initial development of this flow at $Re = 3000$ has been studied experimentally by Bouard & Coutanceau (1980) and numerically by Ta Phuoc Loc & Bouard (1985) and Smith & Stansby (1988). These studies have shown good agreement between calculations and flow visualizations.

A run was made for $Re = 3000$ using $N = 128$ points in the θ-direction and $M = 80$ points in the z-direction with an external radius of $R_\infty = 80$ and a straining parameter of $a = -0.94$. The time step was $\Delta t = 0.001$. Figure 3 shows the calculated development of the separated flow behind the cylinder at five time instant during the initial stages of the flow in which it may be assumed to be symmetrical, and

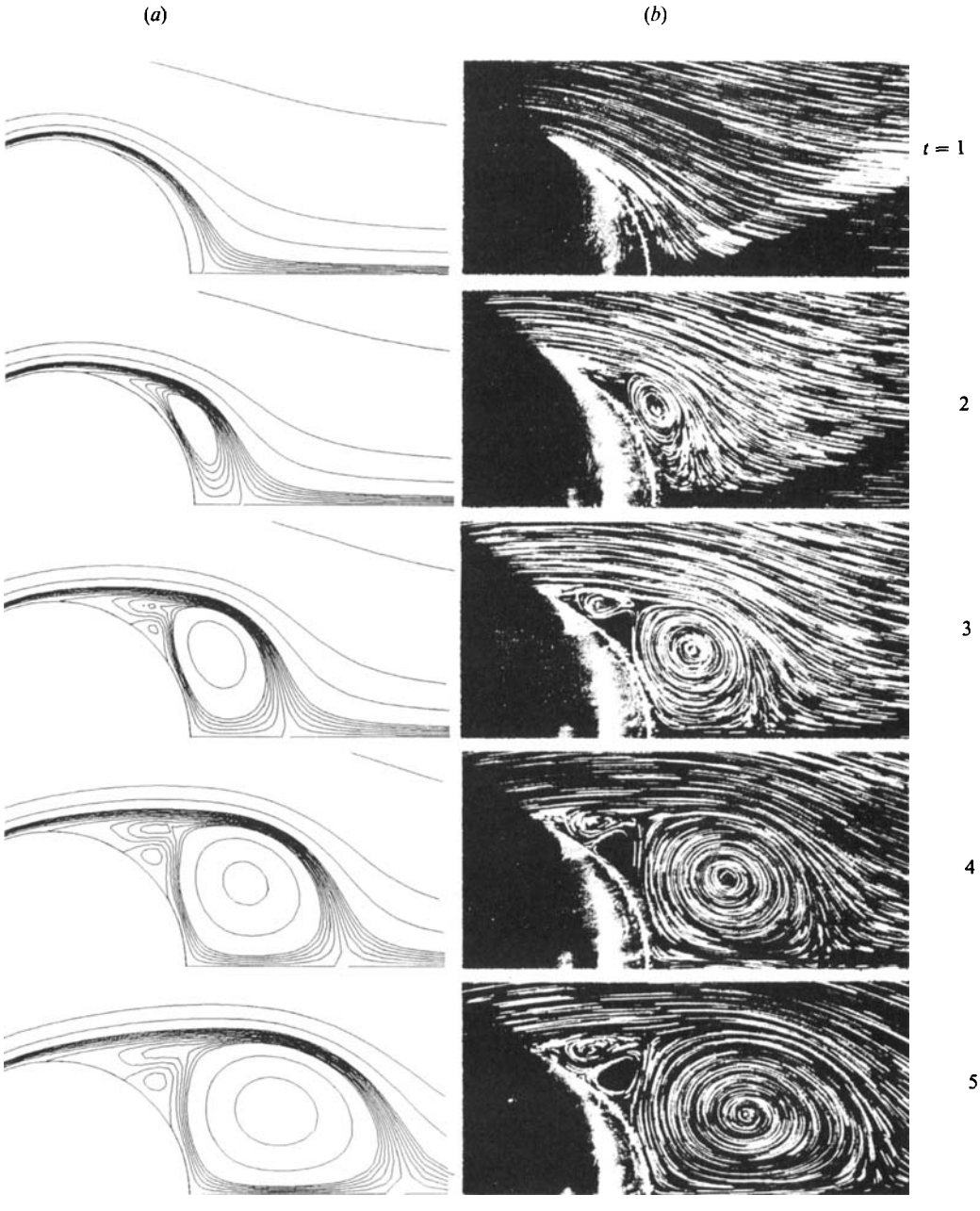

FIGURE 3. Impulsively started flow around a circular cylinder at $Re = 3000$. The development of the separation zone behind the cylinder is depicted for $t = 1, 2, 3, 4$ and 5. (*a*) Present computations visualized by stream-function contours. (*b*) Flow visualization experiment by Bouard & Coutanceau (1980).

turbulence is not important. The agreement between calculated and observed flow field is seen to be excellent. To get a quantitative check of the results from the present code, the reattachment length has been plotted as a function of time in figure 4. The figure also shows results from the other studies. The results from all three numerical models and the experiments show good accordance.

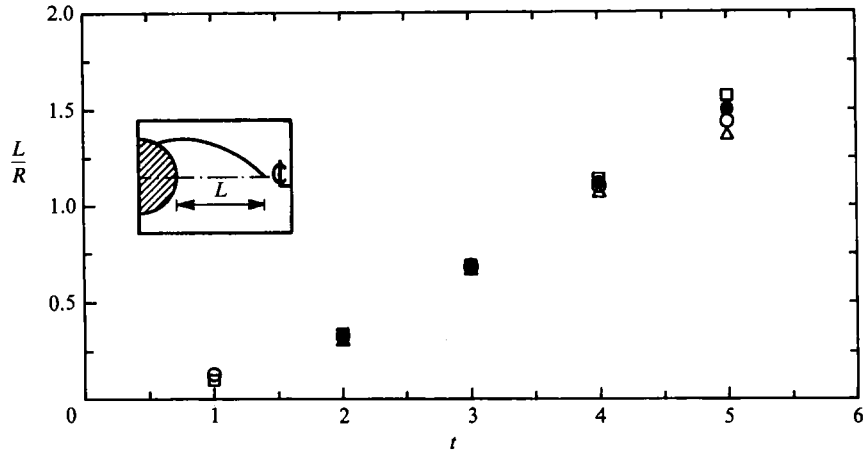

FIGURE 4. Impulsively started flow around a circular cylinder at $Re = 3000$. The reattachment length normalized by the cylinder radius as a function of time. □, Present computations; ○, computations by Ta Phuoc Loc & Bouard (1985); △, computations by Smith & Stansby (1988); ●, experiments by Bouard & Coutanceau (1980).

6. Results

6.1. *General*

The results will be presented in this section, starting with an investigation of the onset of separation and asymmetrical flow. Then the symmetrical flow regime will be studied in terms of flow fields and force coefficients. In the vortex shedding regime, a number of cases representing different modes of vortex shedding will be studied in detail, and finally force coefficients will be presented for the entire interval $0 < KC < 26$ for $\beta = 196$.

The numerical accuracy has been investigated by varying the temporal and spatial resolution as well as the straining in the mesh governed by the parameter a, cf. (8). It has been found that the most important parameter is the straining parameter. It is vital to resolve the flow in the boundary layer, especially in the oscillatory flow in which the large inertia forces must be accommodated for by large gradients in the vorticity near the cylinder surface, cf. (22). As guidance, we have used the boundary-layer thickness of the oscillatory boundary layer over a flat plate (Stokes' second problem) given by (see Rosenhead 1963)

$$\delta = (\pi/\beta)^{\frac{1}{2}}. \tag{25}$$

This flow has a close resemblance with the present flow.

Typically 128 circumferential points and 80 radial points were used. The time step was varied between $\Delta t = 0.001$ and $\Delta t = 0.005$. The straining parameter was $a = -0.94$ for $KC < 6$ and $a = -0.50$ for $KC \geqslant 6$. $R_\infty = 80$ in all simulations. Cases where the numerical parameters deviate from these will be noted.

6.2. *Inception of separation and asymmetrical flow*

Before we can present the results for inception of separation and asymmetrical flow, a short summary of the various phenomena and their related KC- dependency must be given. For a more comprehensive discussion the reader is referred to e.g. Sarpkaya (1986).

Below a certain threshold value of KC, KC_1, the flow remains stable to external disturbances and will remain symmetrical. When this KC is exceeded, the flow is unstable and will become asymmetrical when an external disturbance is introduced. In physical experiments such disturbances will always be present, and the flow will be asymmetrical at KC values larger than KC_i. In the calculations, the flow may remain symmetrical above this threshold value for KC unless an artificial disturbance is introduced. This is because the inevitable numerical dispersion will dampen out any perturbations that could be generated by, e.g. the solution algorithm itself (biased sweep directions in the ADI method etc.). Experiments with the present code have shown that the numerical damping is sufficiently small that asymmetrical flow conditions will develop eventually without artificial triggering. In order to enhance the process, however, we have used the method devised by Martinez (1979) and later used by Braza *et al.* (1986) for inducing an external disturbance. The cylinder is rotated axially in one direction for a period of time followed by a period of rest and a second rotation in the opposite direction.

The asymmetry instability discussed above governs the formation of vortices in the wake of the cylinder, and it must not be confused with the Honji instability (Honji 1981; Sarpkaya 1986) which leads to axially periodic vortices. The Honji instability begins at a critical value KC_{cr} which has been found analytically by Hall (1984). For $\beta = 196$, his solution gives $KC_{cr} = 1.63$. Owing to their intrinsic three-dimensionality these periodic vortices are out of reach of the present two-dimensional model.

According to Sarpkaya (1986), the flow in the boundary layers becomes turbulent at $KC_t \approx 2.8, \approx 2.3$ and ≈ 1.8, for the respective β-values 196, 483, and 1035 (his figure 7). These KC-values are indicative of the maximum KC at which the present laminar code can fully resolve the flow. For KC slightly larger than these values it will be assumed that the flow is only turbulent in parts of the oscillation cycle or in the wake, such that the boundary-layer separation is predominantly laminar.

Separation in relation to the present flow shall be defined as separation in the shear layers with the mathematical definition that the wall shear vanishes. In laminar flow, the normal gradient of the tangential velocity will also vanish at a point in which the wall shear is zero. This definition will imply a breakaway of the surface streamline at the separation point.

6.2.1. *Flow separation*

Calculations have been done to study separation as a function of KC. The migration of the separation point, θ_S, as a function of the phase angle ϕ is depicted in figure 5(*a*) for a series of KC, all for $\beta = 196$. It is seen that in all cases separation occurs at the rear stagnation point at a certain phase angle. The separation point then migrates towards the top of the cylinder and eventually reaches the front stagnation point. This behaviour could be expected, since the rear stagnation point is most susceptible to the effects of the adverse pressure gradient due to the cylinder geometry, which we shall denote P_G.

The phase angle at which separation is initiated varies with the KC. At $KC = 2$, separation initiates at $\phi \approx 75°$. As KC is lowered, the initiation of separation is delayed, and when $KC = 0.2$, the angle is $\phi \approx 128°$. The physical explanation for this can be found by analogy with an impulsively started flow past a cylinder. Here the flow does not separate instantly, because P_G requires time to reverse the flow close to the wall against the external flow direction. The necessary time interval is a function of the time history of the flow. Here it is well known that separation starts

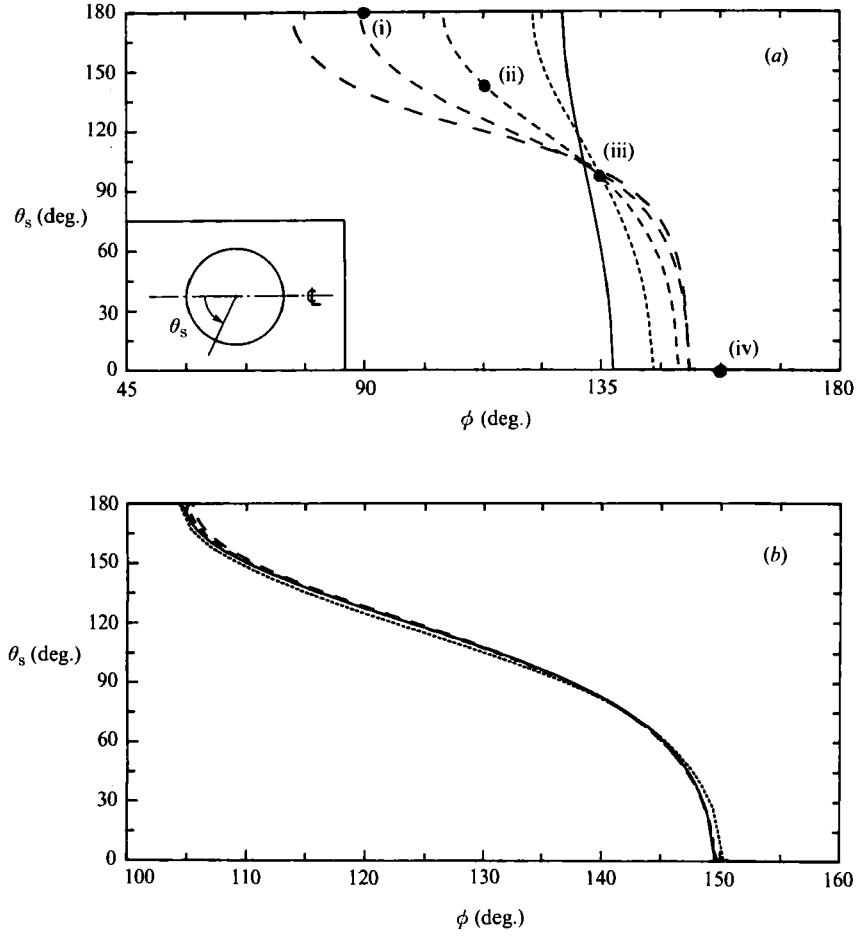

FIGURE 5. Position of the separation point, θ_s, as a function of the phase angle, ϕ, for $\beta = 196$. (*a*) ——, $KC = 0.2$; - - - -, 0.5; – – – –, 1.0; — — — —, 1.5; — — — — — —, 2.0. Numbered large dots indicate points for which flow pictures are given in figure 6. (*b*) Grid refinement study: ——, 128×80, $\Delta t = 0.0025$; · · ·, 64×40, $\Delta t = 0.005$; – – –, 128×80, $\Delta t = 0.001$; — — —, 256×120, $\Delta t = 0.001$.

after the cylinder has moved some distance $s_i = 0.175D$. For a uniformly accelerated cylinder the corresponding distance is $s_u = 0.26D$. As KC increases, so does the amplitude of oscillation, and hence separation will occur earlier in a half-period.

A tempting suggestion would then be to find a limiting KC, KC_S, below which the flow remains unseparated in all phases. If the oscillatory flow is assumed to accelerate uniformly, s_u would correspond to $KC_S = 1.63$. Inspecting figure 5(*a*) we see that even at $KC = 0.2$ separation occurs, and therefore KC_S is much lower than 1.63, at least for $\beta = 196$. The explanation is that the flow can be assumed to accelerate uniformly only in a small part of the cycle, but much more important is that the presence of an external pressure gradient P_E in oscillatory flow causes a reversal of the entire flow twice every period.

From the theory for the oscillatory boundary layer over a flat plate, Stokes' second problem, it is known that the reversal of the wall shear stress occurs at $\phi = 135°$, i.e. the wall shear leads the external velocity by 45°. Furthermore, the leading term for

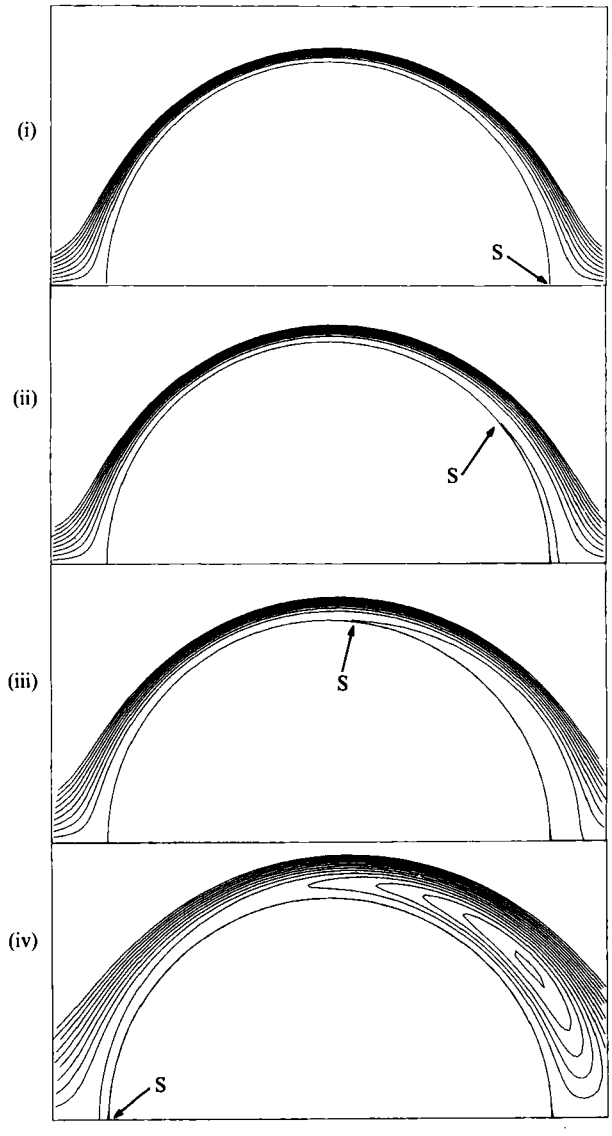

FIGURE 6. Computed flow fields for $KC = 1$ and $\beta = 196$. Stream-function contours, $\psi_{\min} = -0.05$, $\psi_{\max} = 0.05$, $\Delta\psi = 0.005$. The separation points are marked with an S. (i) $\phi = 90°$; (ii) 112.5°; (iii) 135°; (iv) 157.5° (see figure 5*a*).

the friction force in the theory by Wang (1968) which is valid for $KC \ll 1$ also gives a reversal of the wall shear at 135°. It may therefore be expected that in the limit as KC tends to zero the reversal of the wall shear stress will occur almost simultaneously over the entire cylinder. In the model we see this as the separation point moving from the rear stagnation point to the front stagnation point at $\phi \sim$ 135°. From a physical point of view it can be argued that as $KC \to 0$ the flow amplitude will become so small (with respect to the cylinder diameter) that the flow will not be able to feel the geometry of the wall below it, whether the wall is a cylinder surface or a flat plate, i.e. P_E becomes much more important than P_G. Thus the

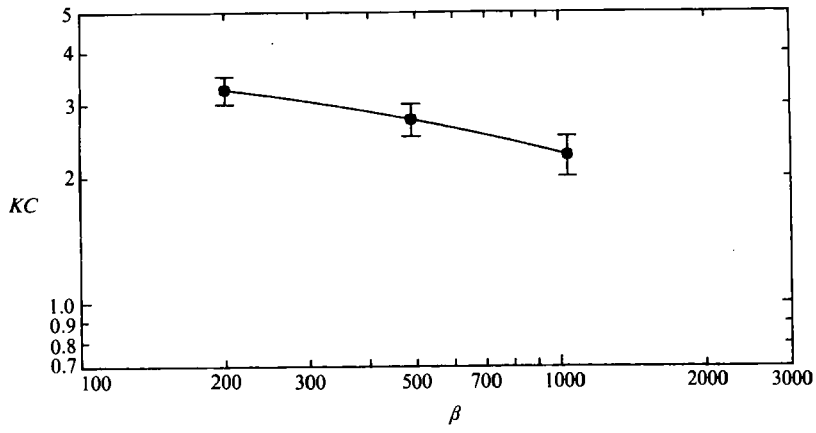

FIGURE 7. Inception of asymmetrical flow. —•—, Inception of asymmetrical flow computed by the present code; error bar indicates the lower and upper limits, i.e. the flow is found to be stable at the lower limit and found to be unstable at the upper limit.

separation phenomenon will lead to simultaneous flow reversal over the entire cylinder surface. The results in figure 5(*a*) indicate such a trend.

No attempt has been made in the present study to investigate the approach to simultaneous flow reversal. This is because the numerical solution becomes more difficult to obtain in this region owing to the fast oscillations.

In order to illustrate the flow fields and further support the arguments above, we have depicted a series of flow pictures in the form of stream-function contours in figure 6 for $KC = 1$ and $\beta = 196$. The four pictures show the progressive development of separation followed by flow reversal. The time instances for the four pictures are marked on figure 5(*a*) for easy reference.

Experiments reported by Sarpkaya (1986) suggest that the onset of separation occurs in the interval $1.5 < KC < 3$, depending somewhat on β. The previous results show that separation, according to the present definition, has already occurred at much lower KC, at least in a two-dimensional flow. As noted by Sarpkaya (1986), the experimental determination of separation is subjective, owing to a number of difficulties associated with flow visualization. We think that, most likely, separation must develop up to a certain stage before it can be observed in the experiments.

To investigate whether the chosen grid was fine enough to ensure that the effects of numerical viscosity were negligible, the case $KC = 1$ and $\beta = 196$ was analysed with four different grids and time steps. The influence of discretization on the migration of the separation point is shown in figure 5(*b*). It is seen that the chosen grid, indicated by a solid line, is sufficiently free from artificial viscosity for the results to be trustworthy.

6.2.2. *Asymmetrical flow inception*

In figure 7, a curve with 'error bars' shows the region in the (KC, β)-plane in which the flow becomes unstable and thus asymmetrical according to the present model. The bars do not indicate a standard deviation, but they show a lower and an upper limit for the instability. We do not give precise values for KC_1, because its determination is based on the inspection of the temporal growth of the transverse force on the cylinder. The computations would have to be carried out for very long time intervals to obtain a very accurate threshold value. Furthermore, this value

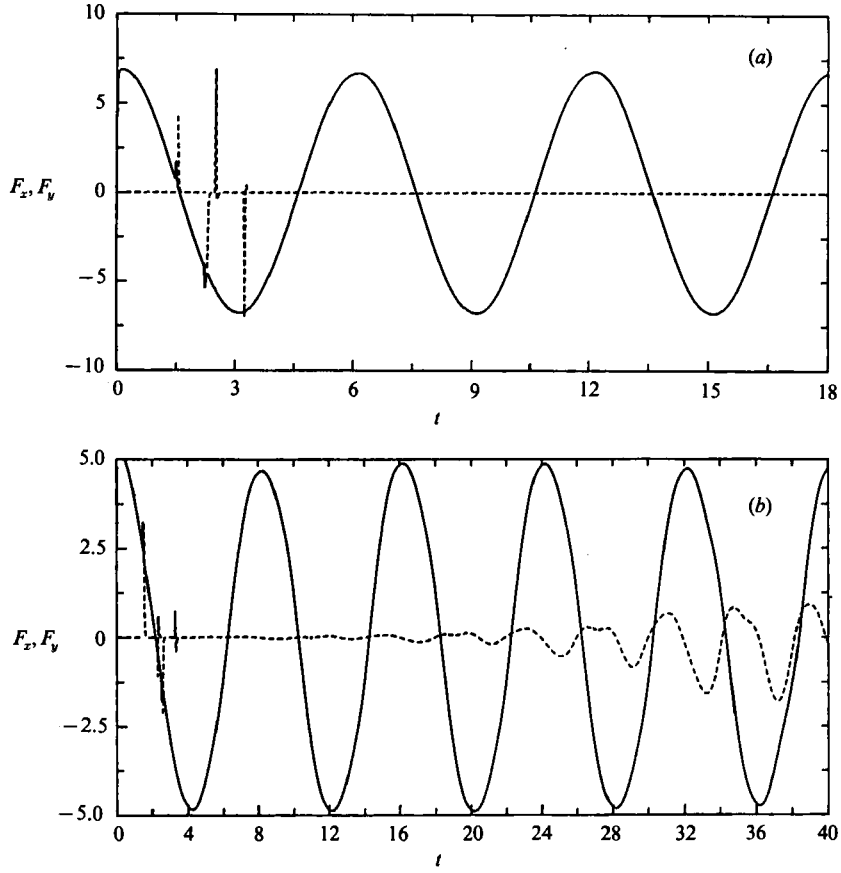

FIGURE 8. Force traces for $\beta = 196$. To introduce a disturbance in the flow, the cylinder has been rotated in the interval $2 < t < 2.5$ with a velocity of $V = 0.30$ at the wall, and in the interval $2.75 < t < 3.25$ with a velocity $V = -0.20$. ——, In-line force; — — — —, lift force. (*a*) $KC = 3$; (*b*) $KC = 4$.

would be affected by the numerical viscosity. An example of the computed force traces for a perturbed flow ($KC = 3, \beta = 196$) is given in figure 8(*a*). It is seen how the lift force attains very large values while the disturbances are applied. Later, the lift force dampens out, and we conclude that in this particular case, the flow is stable. Figure 8(*b*) shows an unstable case ($KC = 4, \beta = 196$).

Little is known from experiments about KC_1 and its functional behaviour with β. Williamson (1985) and Obasaju, Bearman & Graham (1988) have reported that asymmetrical flow is initiated at $KC_1 \approx 4$. The observations are based on flow visualizations and transverse force measurements.

6.3. *Symmetrical flow*

This section will deal with the computed flow fields and forces on the cylinder in the region $0 < KC < KC_1$, where we can consider the flow to be symmetrical, as shown in the previous section.

6.3.1. *Flow fields*

In this section we shall compare computed flow fields with flow visualization experiments that were carried out to provide flow pictures at small KC and small Re

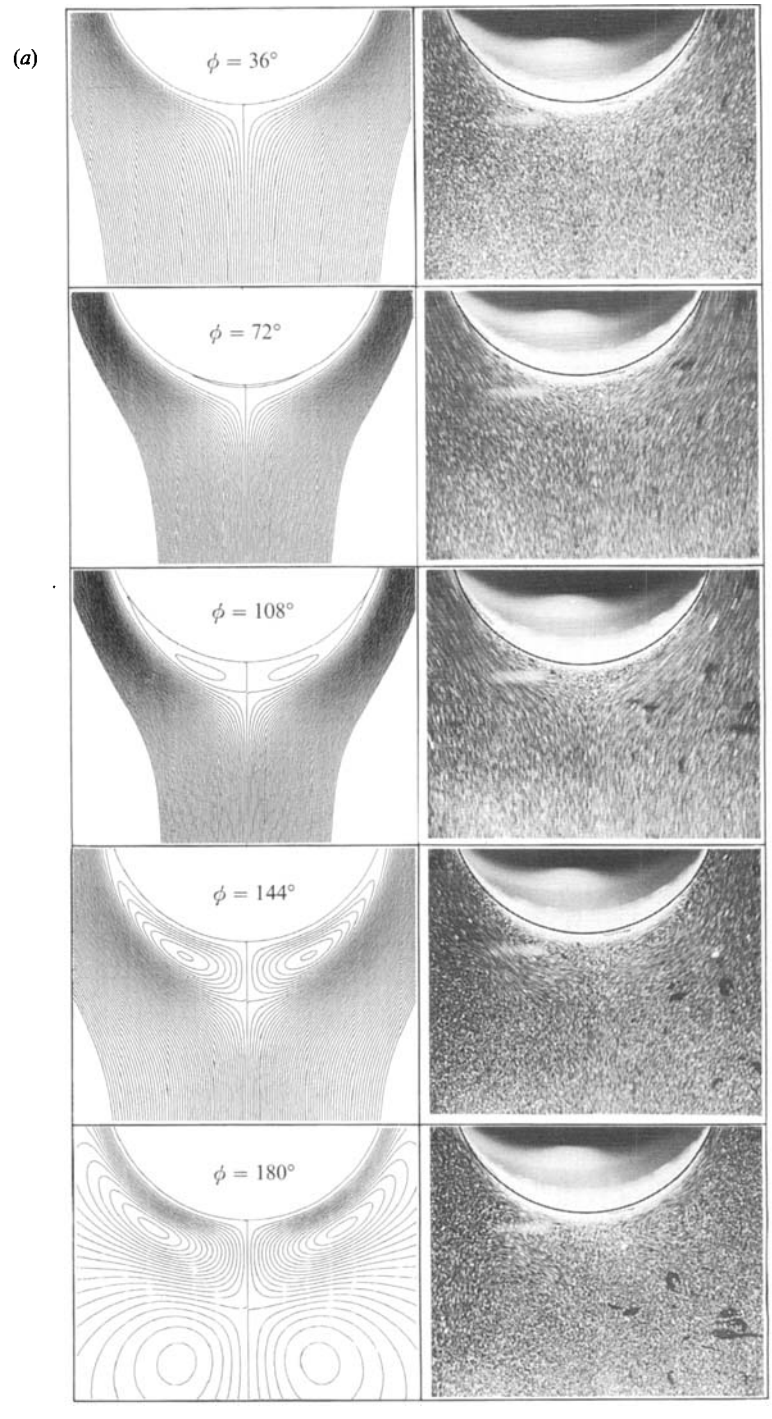

FIGURE 9. $KC = 2.2$, $\beta = 250$. (*a*) Computed instantaneous contours of the stream function, ψ; $\psi_{\min} = -0.5$, $\psi_{\max} = 0.5$, $\Delta\psi = 0.01$. (*b*) Flow visualization. Five instances from one half-period are shown.

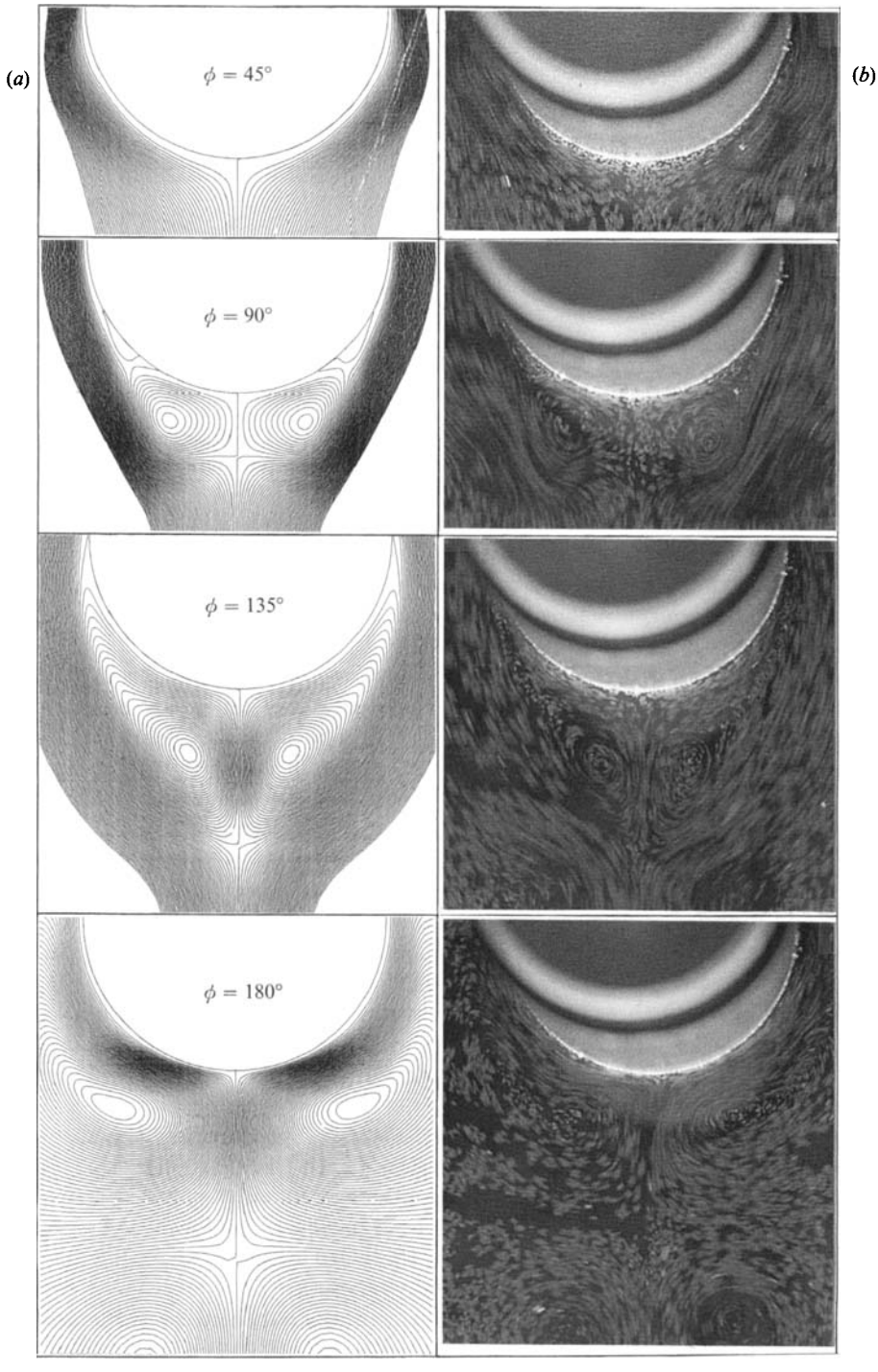

FIGURE 10. $KC = 4.0$, $\beta = 250$. (*a*) Computed instantaneous contours of the stream function, ψ; $\psi_{\min} = -0.5$, $\psi_{\max} = 0.5$, $\Delta\psi = 0.01$. (*b*) Flow visualizations. Four instances from one half-period are shown.

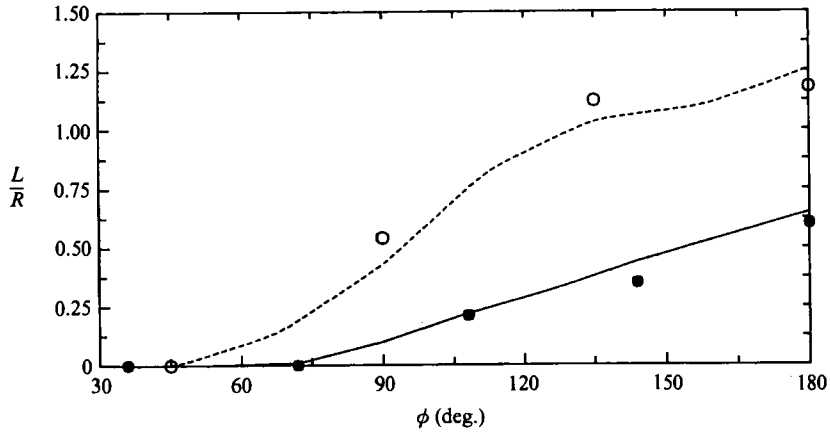

FIGURE 11. The length of the separation bubble as a function of the phase angle, ϕ. ——, Present code, $KC = 2.2$; ●, present experimental results taken from photographs, $KC = 2.2$; – – –, present code, $KC = 4.0$; ○, present experimental results taken from photographs, $KC = 4.0$. $\beta = 250$.

in a regime in which the model can give results which are fully or almost fully resolved. In these computations we have used 256 circumferential points and 180 points in the radial direction, and $a = -0.50$, $R_\infty = 20$.

Figure 9(*a*) depicts five computed flow fields for $KC = 2.2$ and $\beta = 250$ during one half-cycle of oscillation. Isolines of the total stream function, ψ, are used to illustrate the instantaneous flow patterns, and only one side of the cylinder is shown. The corresponding flow visualization pictures are given in figure 9(*b*). The figure shows how a symmetrical pair of counter-rotating vortices is formed during the half-cycle. Two surviving eddies from the previous half-cycle are washed over the cylinder to form a pair of eddies rotating in the opposite direction compared with the newly formed ones. In this case, the computations are confirmed by the visualizations.

At $KC = 4.0$ and $\beta = 250$ the computations give the same qualitative results in terms of vortex formation and movements, as shown by the stream-function isolines in figure 10(*a*). Again good accordance with the visualizations in figure 10(*b*) is seen. Although the pictures show a weak asymmetry, we have included this case in the present section and compared the experimental results with a symmetrical computation. The results from both sources stem from the initial periods of oscillation.

The pictures allow a quantitative comparison by considering the reattachment length as a function of time and KC. In figure 11 we have depicted this length as a function of the phase angle, ϕ, for the two values of KC at $\beta = 250$. The comparison shows that the temporal development of the separation bubble is well predicted by the code in both cases. We also note that the separation bubble becomes larger at $KC = 4$ than at $KC = 2.2$, which was to be expected.

Finally we compare flow pictures with the pictures obtained by Williamson (1985) for $KC = 4$ and presumably $\beta = 1020$. Figure 12 depicts the computed flow fields in terms of isolines of the 'viscous' part of the stream function, ψ_v, which gives flow pictures in a frame of reference fixed relative to the water tank and thus the same as used by Williamson in his pictures. The computation indicates that the vortex movement is qualitatively the same as found for the lower β-value in our own visualizations, whereas Williamson's pictures clearly show that in each half-cycle

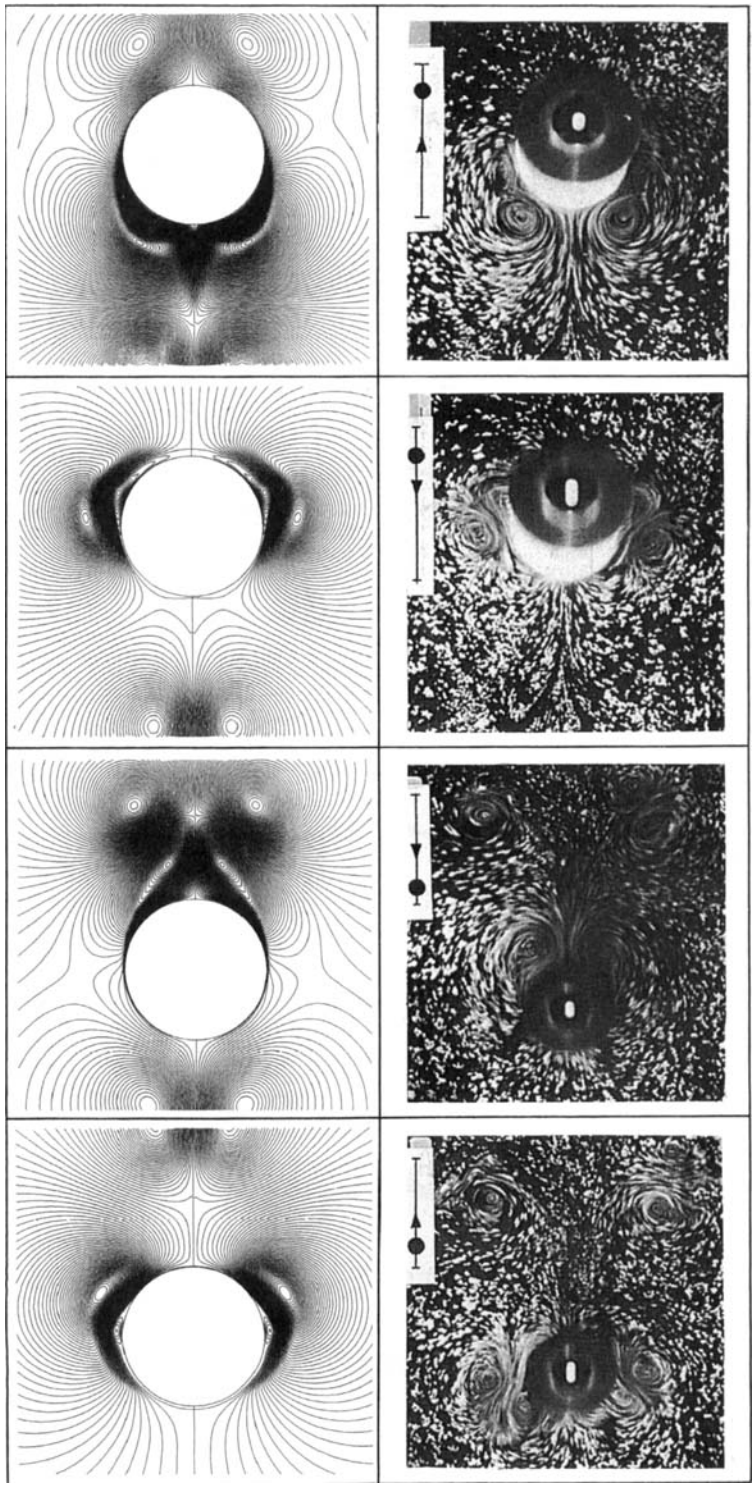

FIGURE 12. $KC = 4.0$, $\beta = 1020$. (*a*) Computed instantaneous contours of the viscous part of the stream function, ψ_v; $\psi_{v,\min} = -0.9$, $\psi_{v,\max} = 0.9$, $\Delta\psi_v = 0.01$. (*b*) Flow visualizations from Williamson (1985).

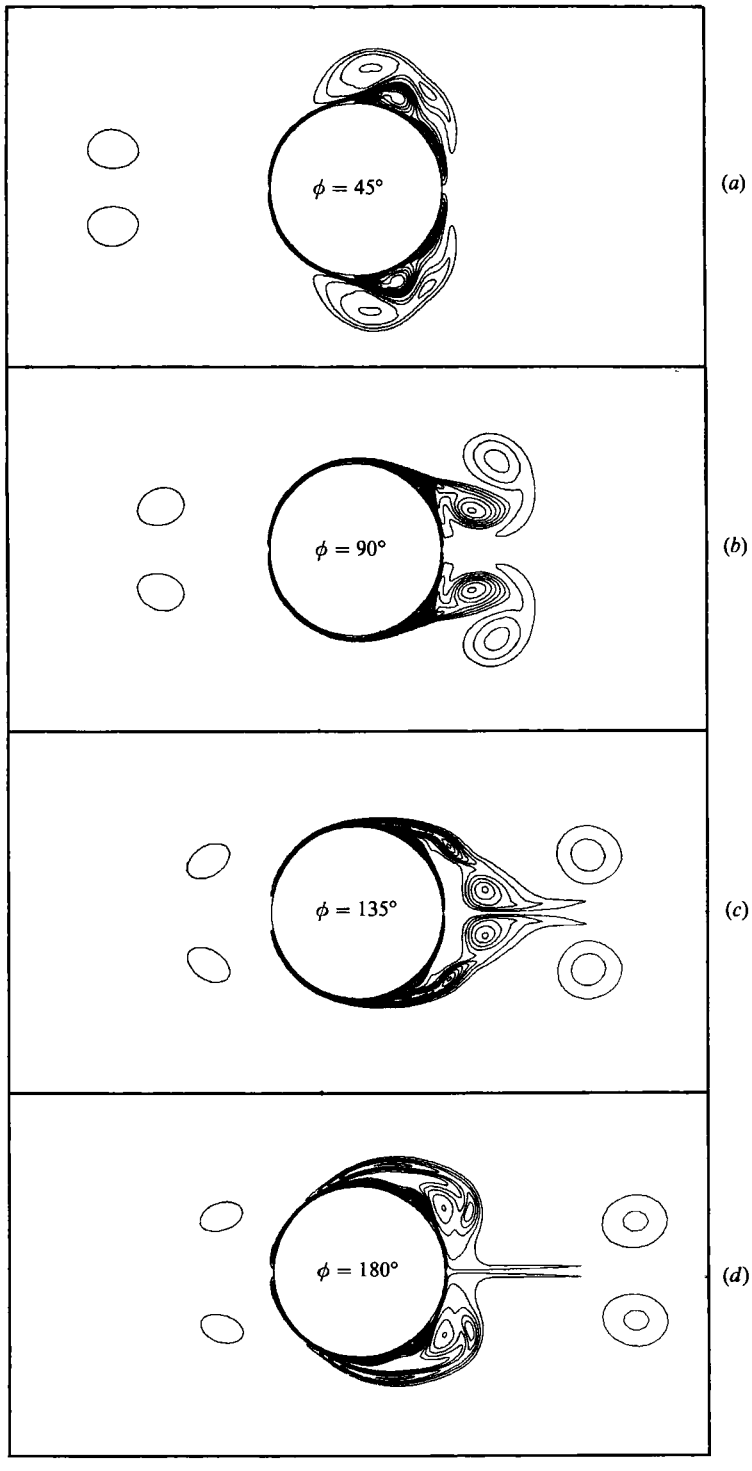

FIGURE 13. $KC = 4.0$, $\beta = 1020$. Computed instantaneous contours of the vorticity, ω; $\omega_{\min} = -50$, $\omega_{\max} = 50$, $\Delta\omega = 2$.

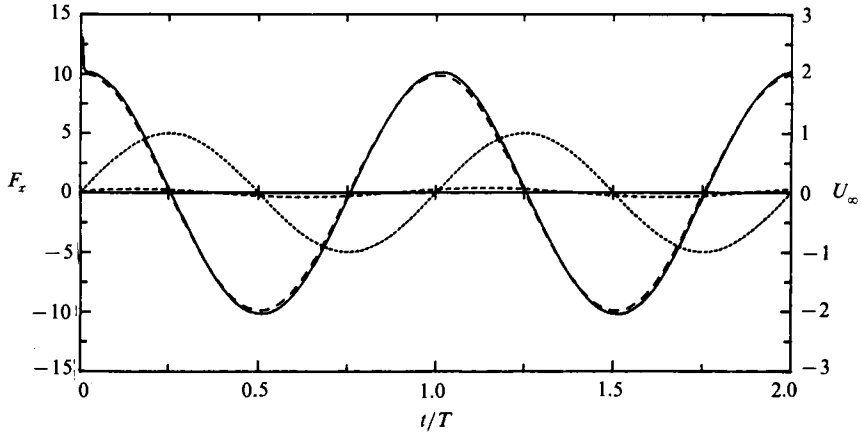

FIGURE 14. Computed in-line force traces for $KC = 2$ and $\beta = 483$ during two periods of oscillations: ——, total in-line force; — — — —, pressure part of in-line force; – – – –, friction part of in-line force: · · · · · ·, external velocity.

two vortex pairs are formed and detached from the cylinder as the cylinder reverses direction. In the first two pictures in figure 12 it can be seen that, in the computation, the eddies are washed over the cylinder as the flow is reversed and an interaction with the newly forming eddies on the opposite side of the cylinder takes place. It appears, however, that the strengths of the surviving eddies are not sufficient in order to detach the vortex pairs. Instead the pairs are forced behind the cylinder, which can be seen in the third picture. As the flow reverses direction, only the new vortices are washed over the cylinder again, thus closing the cycle. The vorticity plots in figure 13 give another illustration of the vortex movements.

The explanation for the discrepancy is likely to be found in the difference in Re between our experiments and that by Williamson. The reason why the model does not predict the difference must be explained by artificial viscosity, which will play a larger role as Re is increased, and the fact that the model has a poor resolution at higher Re.

6.3.2. *Forces*

As an example, the in-line force traces for $KC = 2$ and $\beta = 483$ are depicted in figure 14. The total force is almost sinusoidal because of the inertia forces, and it is dominated by the pressure forces. The friction force trace clearly shows a 45° lead over the external velocity as discussed in §6.2.

A grid refinement study similar to the one reported in §6.2.1 confirmed the earlier result that the chosen grid is sufficient.

We shall now reduce the computed forces to force coefficients. In steady flow (24*a*) and (24*b*) give the usual drag and lift coefficients, respectively. In unsteady flows, there will be an inertia force acting on the cylinder in the flow direction due to the fluid acceleration. The inertia force is usually split into two parts: the Froude–Krylov force, which is due to the far-field pressure gradient; and the inertia force due to 'added mass' arising because of the local acceleration near the cylinder. Both contributions are included in F_x as determined by (24*a*). It is desirable to separate the inertia and drag forces. In oscillatory flow it is usual to describe the in-line force by

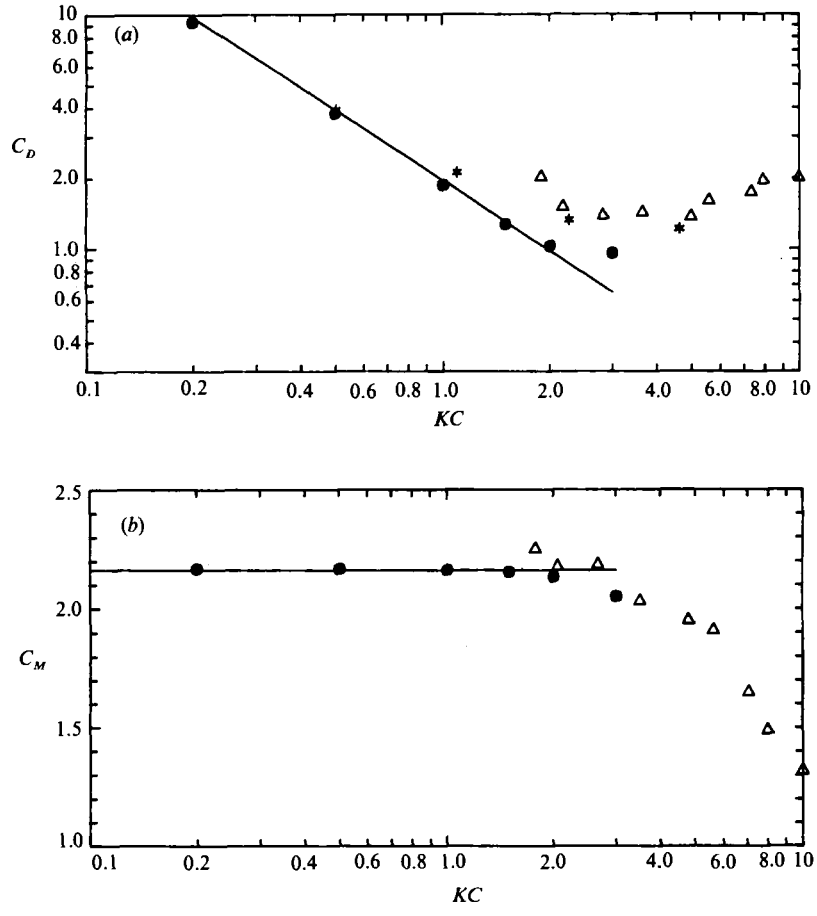

FIGURE 15. Force coefficients as a function of KC for $\beta = 196$. ●, Present code; *, discrete vortex method by Graham & Djahansouzi (1989); △, experiments by Bearman *et al.* (1985); ——, asymptotic theory by Wang (1968). (*a*) Drag coefficient; (*b*) inertia coefficient.

the Morison equation (Morison *et al.* 1950) which assumes that the force per unit length is given as a linear sum of the inertia and drag forces as

$$F_x^* = \tfrac{1}{4}\rho\pi D^{*2} C_M \frac{\mathrm{d}U_\infty^*}{\mathrm{d}t^*} + \tfrac{1}{2}\rho D^* C_D U_\infty^* |U_\infty^*|. \tag{26}$$

In dimensionless form we have

$$F_x = \pi C_M \frac{\mathrm{d}U_\infty}{\mathrm{d}t} + C_D U_\infty |U_\infty|. \tag{27}$$

Inertia coefficients and drag coefficients due to pressure and friction may be determined by the usual least-square-fit method or Fourier averaging, which are well known from the processing of experimental force time series.

The choice of β-values for which force coefficients will be presented in the following has been governed by the available experimental data. Figures 15–17 depict drag and inertia coefficients for $\beta = 196$, 483 and 1035, respectively. From figure 15 it is seen that for $\beta = 196$ the computed coefficients for $KC \leqslant 1.5$ are in excellent agreement

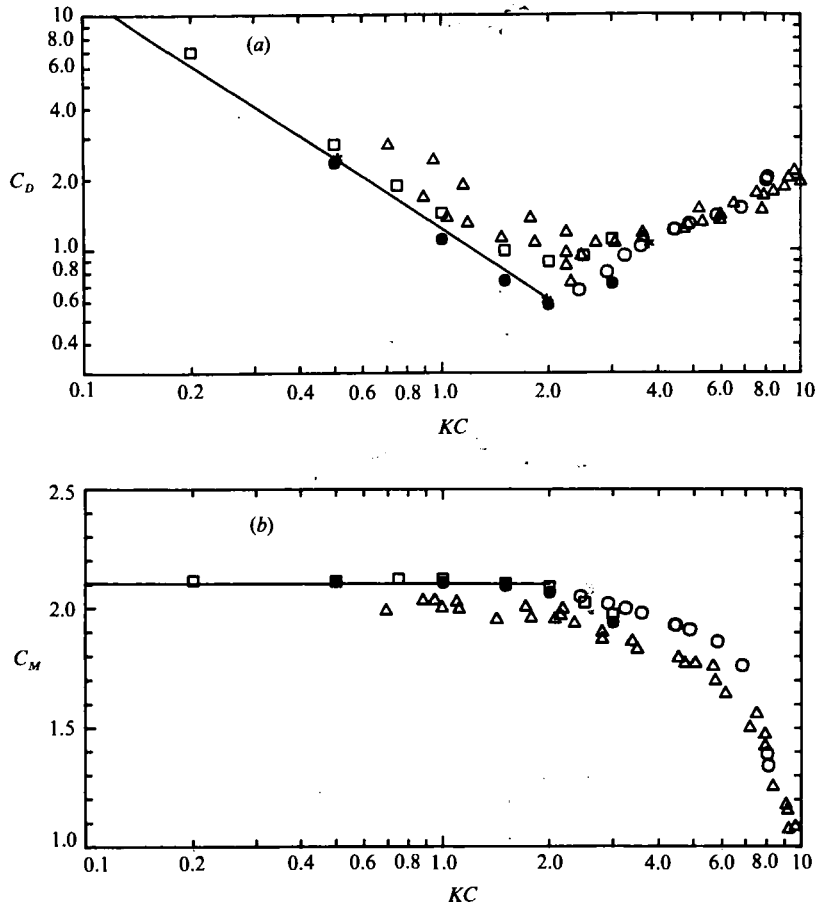

FIGURE 16. Force coefficients as a function of KC for $\beta = 483$. ●, Present code; *, discrete vortex method by Graham & Djahansouzi (1989); □, discrete vortex method by Stansby & Smith (1989); △, experiments by Bearman *et al.* (1985); ○, experiments by Sortland (1986); ——, asymptotic theory by Wang (1968). (*a*) Drag coefficient; (*b*) inertia coefficient.

with the analytical theory by Wang (1968), which is an asymptotic theory that assumes attached flow and is valid for $KC \ll 1$ and $\beta \gg 1$. As KC is increased, C_D decreases but departs from Wang's solution owing to the increasing effects of flow separation in the boundary layers and the formation of eddies, cf. for example figures 10 and 11. C_D reaches a minimum at $KC \sim 3$. The experimental values for C_D (Bearman *et al.* 1985) are generally higher than both the present data and the theory by Wang. A possible explanation is the absence of the Honji instability in the model. The drag coefficients obtained by Graham & Djahansouzi (1989) from a discrete-vortex model are also larger than the present ones. Since the bases for both numerical models are similar, this discrepancy must be related to the numerical methods. Figure 15(*b*) show a very good agreement between computed and experimental values of C_M. The decrease from the Wang solution as KC is increased is very well predicted.

For $\beta = 483$, C_D is slightly underpredicted by the code compared to the theory by Wang, cf. figure 16(*a*). The behaviour of the model results in relation to the experimental data provided by Bearman *et al.* (1985) and Sortland (1986) is similar

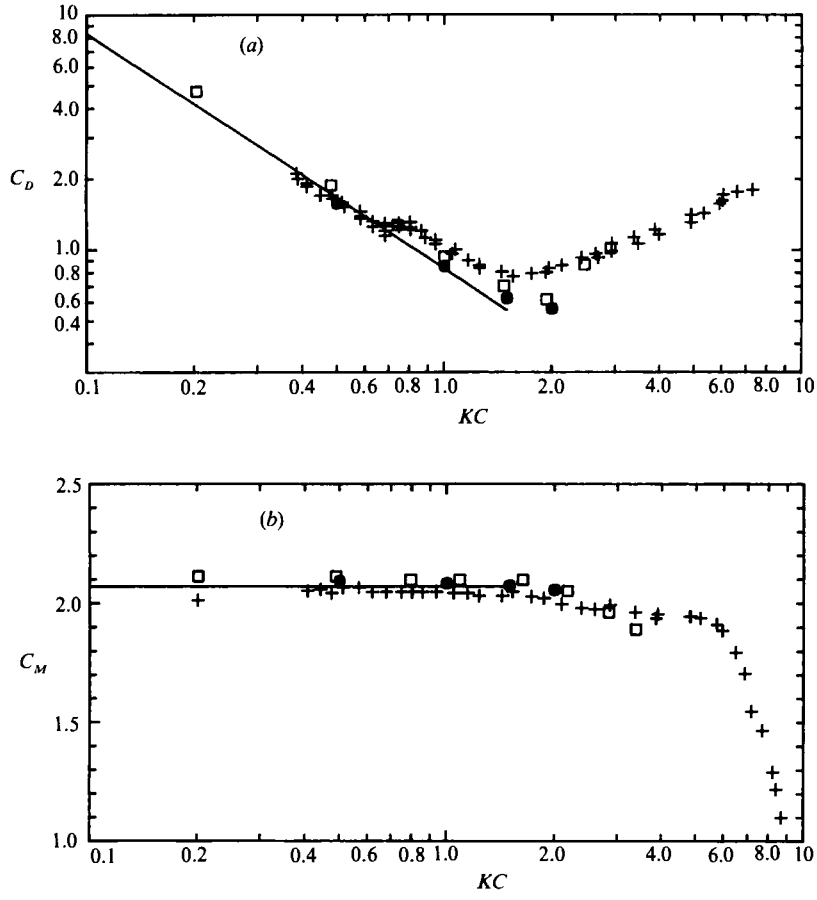

FIGURE 17. Force coefficients as a function of KC for $\beta = 1035$. ●, Present code; □, discrete vortex method by Stansby & Smith (1989-; +, experiments by Sarpkaya (1986); ——, asymptotic theory by Wang (1968). (*a*) Drag coefficient; (*b*) inertia coefficient.

to that found for $\beta = 196$. The agreement with the discrete-vortex method results by Graham & Djahansouzi (1989) is much better than in the case $\beta = 196$. The discrete-vortex-method results by Stansby & Smith(1989) give somewhat higher values for C_D. The reason for the latter discrepancy is not known. The calculated C_M-values (figure 16*b*) agree very well with those found by Stansby & Smith (1989). The experimental values for C_M from Bearman *et al.* (1985) and Sortland (1986) are respectively below and above the theoretical predictions.

Figure 17 shows drag and inertia coefficients for $\beta = 1035$ and includes the present computational data together with data from Stansby & Smith (1989) and experimental data by Sarpkaya (1986). The results are similar to those found for $\beta = 483$. In figure 17(*a*), the experimental data show, as noted by Sarpkaya, the inception of the Honji instability at $KC_{cr} \sim 0.75$ which leads to an increase of C_D. This effect is not – and should not be expected to be – captured by the two-dimensional models. At $\beta = 1035$, Sarpkaya (1986) has found that the onset of turbulent flow occurs at $KC_t \sim 1.8$. Therefore, model results for larger values of β are not fully resolved.

To close this section we present in figure 18 the drag coefficient for $\beta = 196$ as in

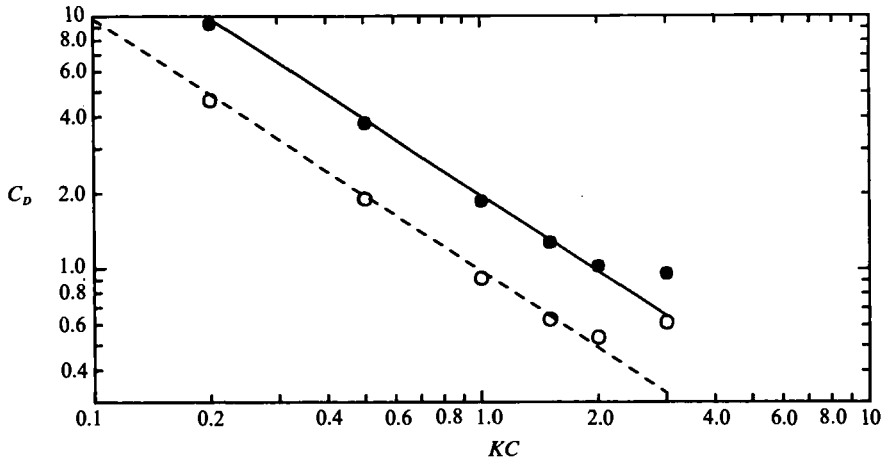

FIGURE 18. Drag coefficients as a function of KC for $\beta = 196$. ●, Total drag by present code; ○, pressure drag by present code; ——, total drag from asymptotic theory by Wang (1968); – – –, pressure drag from asymptotic theory by Wang (1968).

figure 15(a), but this time we have separated the pressure part of the drag, i.e. drag from the first term in (24a). It can be shown that the pressure and friction forces each account for half of the drag force in this regime. The figure shows that there is an excellent agreement between the asymptotic theory and the numerical model on this aspect.

6.4. *Vortex shedding regimes*

6.4.1. *General*

As described in the introduction, the existence of some very distinct vortex shedding regimes for the oscillatory flow around a circular cylinder at small KC is now well established. Several experimental investigations have shown these vortex patterns (Maull & Milliner 1978; Bearman *et al.* 1981; Bearman 1985; Williamson 1985). The theoretical study of these patterns will, owing to their complexity, have to be made by numerical models. A few attempts have been reported in the literature (Stansby 1979; van der Vegt & de Boom 1985; Skomedal *et al.* 1989; Baba & Miayata 1987; Murashige *et al.* 1989). The first three of these models were discrete vortex models, whereas the last two were Eulerian finite-difference models. Sarpkaya (1989) has given an excellent review and assessment, of especially, the vortex models.

In the present work we have chosen to keep the Reynolds number relatively small ($\beta = 196$) in the study of the vortex patterns, such that the effects of transition and turbulence remain as small as possible. The highest KC-value that will be discussed is 26. Although the model can produce results for higher values, the investigation was stopped at this point, because the above-mentioned effects would become increasingly important and thus render the results less interesting.

In the following we shall present and discuss the results that have been obtained for four different vortex shedding regimes encountered in the interval $7 < \mathrm{KC} < 26$. These are the 'transverse street', the 'single pair', 'the double pair' and the 'three pair' regimes as classified by Williamson (1985). In each case we shall look at the computed flow fields and force traces over a period of oscillation. We shall refer to the first and second half-periods of oscillation, meaning respectively the time intervals $0 < \phi < \pi$ and $\pi < \phi < 2\pi$. In all calculations we have used the perturbation method described in §6.2 to initiate vortex shedding early in the calculation.

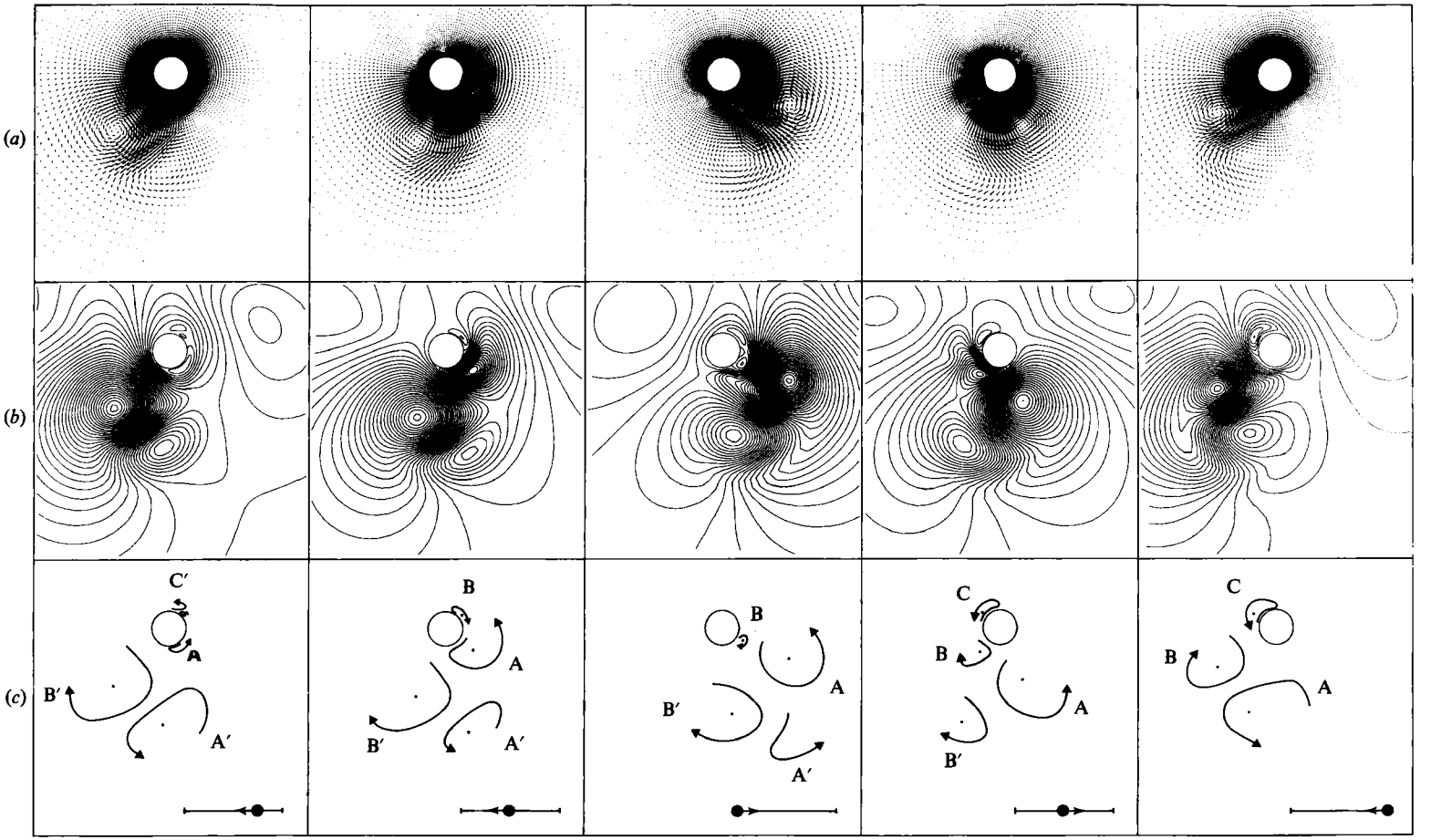

FIGURE 19. Computed flow fields for $KC = 8$ and $\beta = 196$. (*a*) Velocity vectors derived from ψ_v. (*b*) Stream-function contours; the cylinder is assumed to oscillate in still water, and the frame of reference is that of the still water, $\psi_{min} = -6$, $\psi_{max} = 6$ and $\Delta\psi = 0.075$. (*c*) Sketches showing the vortex patterns indicating vortex centres and direction of rotation which may be observed in (*a*) and (*b*); the arrow in the lower right corner indicates the direction of the cylinder motion, and the position of the cylinder on the axis shows the time phase. Five instances are shown: $\frac{1}{4}\pi$, $\frac{1}{2}\pi$, π, $\frac{3}{2}\pi$ and 2π.

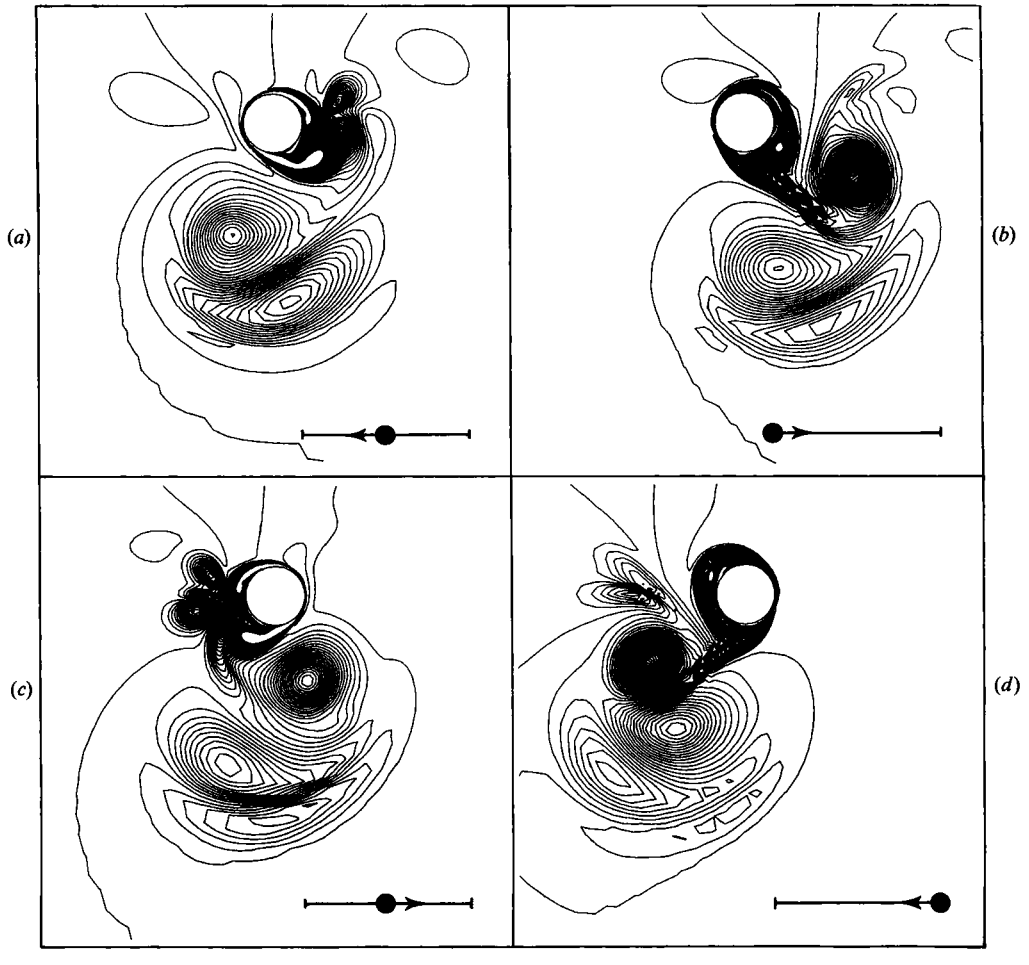

FIGURE 20. Computed vorticity contours for $KC = 8$ and $\beta = 196$. Four instances are shown: (*a–d*) $\frac{1}{2}\pi$; π; $\frac{3}{2}\pi$ and 2π respectively. $\omega_{\min} = -5$, $\omega_{\max} = 5$ and $\Delta\omega = 0.1$.

6.4.2. *Transverse street*

The first vortex shedding regime to be encountered in the asymmetrical flow for KC larger than ≈ 7 is the so-called 'transverse street', which takes its name from the fact that a pair of vortices generated in each cycle of oscillation advects away from cylinder in a direction almost perpendicular to the main flow direction. This one-sided vortex shedding gives rise to a non-zero mean transverse force (Bearman *et al.* 1981; Williamson 1985). The present example is that of $KC = 8$ and $\beta = 196$ for which this flow pattern has been found to be dominating.

In figure 19 the flow fields, which are illustrated by velocity vectors and contours of the stream function, show how the vortices are generated and move to one side of the cylinder. The sketches show the centres of the main vortices and their direction of rotation.

Owing to the action of viscosity the lifetime of the vortices is limited. Therefore we see a fast destruction of the vortices as they move away from the cylinder. Note that the influence of the numerical viscosity increases away from the cylinder since the

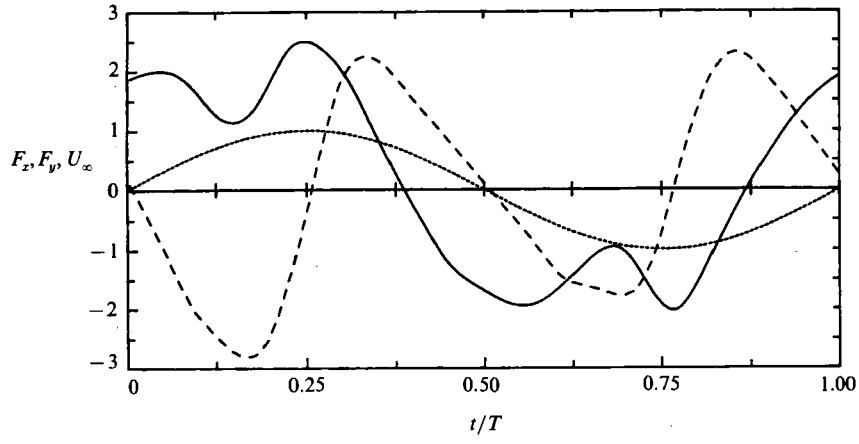

FIGURE 21. Computed force traces over one period of oscillation for $KC = 8$ and $\beta = 196$: ——, in-line force; – – –, transverse force; · · ·, external velocity.

grid spacing becomes larger and larger. Contour plots of the computed vorticity field as depicted in figure 20 also show that the vortices survive only for a few periods of oscillation. The very steep gradients in vorticity and thus the need for a very fine grid near the cylinder are seen clearly in figure 20.

The mechanics of the transverse street, in which the cylinder constantly reverses into the wake which was formed in the prior half-period, and the resulting vortex pairing seen in figures 19 and 20 are in excellent agreement with the experimental observations made by several investigators at $KC \approx 8$. See Williamson (1985) for a detailed description of the mechanics of the formation of this vortex pattern.

As discussed by for example Maull & Milliner (1978) the shedding and return of the vortices create a very characteristic transverse force trace. In figure 21 the computed in-line and transverse force traces for $KC = 8$ are depicted together with the external velocity variation over one cycle of oscillation in which the transverse street shedding occurs. As would be expected from the experimental investigations, the frequency of the transverse force is two times the basic frequency of oscillation. Figure 21 also shows that the transverse force is larger in magnitude than the in-line force.

6.4.3. *Single pair*

The calculation for $KC = 12$ depicted in figure 22 may be interpreted as being in the so-called 'single-pair' regime which, according to Williamson (1985), succeeds the transverse street, as KC is increased. Figure 22 reveals that the vortex street now forms an angle of roughly 45° with the main flow direction. This can be explained by the increased amplitude of oscillation caused by the larger KC. The vortex patterns are similar in principle, which may also be seen by comparison of figure 19 with figure 22. As a result of the increased KC in figure 22, there is more time in each half-period for the creation of vorticity and hence the vortices are larger when the flow reversal occurs. Compare vortex C of figure 19 with vortex D of figure 22. The transition from the transverse street to the single-pair regime is not abrupt at a critical value of KC, but must be considered to take place gradually in terms of the KC value, thus 'turning' the wake gradually from $\approx 90°$ to $\approx 45°$.

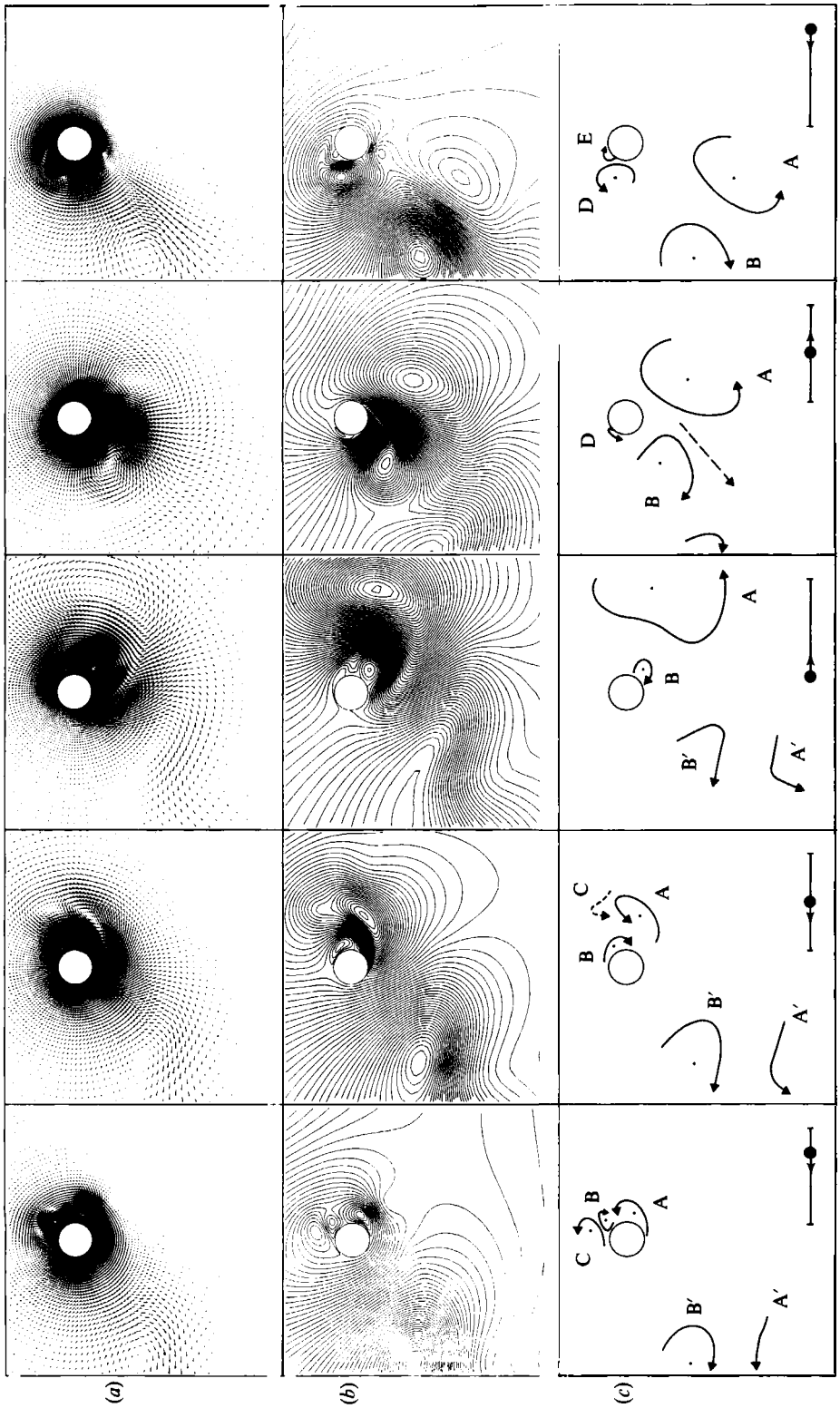

FIGURE 22. Computed flow fields for $KC = 12$ and $\beta = 196$. See figure 19 for a description.

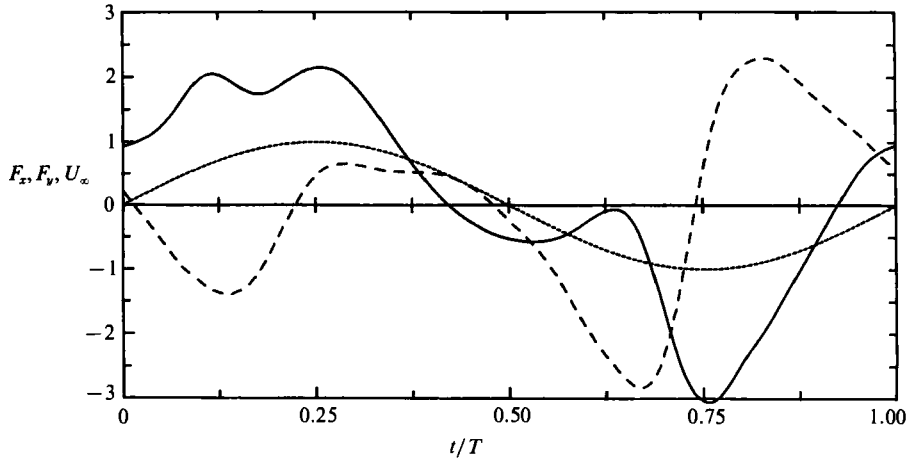

FIGURE 23. Computed force traces over one period of oscillation for $KC = 12$ and $\beta = 196$; ——, in-line force; – – –, transverse force; · · ·, external velocity.

The force traces depicted in figure 23 are almost identical to those in figure 21 for $KC = 8$. The main difference is the smaller positive peak for the transverse force during the first half-period. Williamson (1985) has also found in his experiments that the peaks become uneven in size in the single-pair regime. The fundamental frequency of the transverse force is still two times the oscillation frequency, and the in-line and transverse forces are still similar in magnitude.

In contrast to the experience from experiments (Williamson 1985; Obasaju *et al.* 1988) which says that the transverse street and the single-pair regimes are very stable regimes that, once established, will remain for a number of periods, the present computations have not shown the same persistency. It is obvious that large secondary currents are present in the flow in order to compensate for the mass flux in the transverse street, thus making the interaction between the near-cylinder flow and the far-field large-scale flow very important. Perhaps this interaction is not sufficiently accounted for by the model.

6.4.4. *Double pair*

At a certain KC-value, the vortices D and E in figure 22 become so well developed during the second half-period that, after flow reversal, they are shed as a vortex pair and hence the 'double-pair' regime is a reality. Here two pairs of vortices are shed during each cycle of oscillation. In figure 24 we have depicted the calculated flow field for $KC = 18$ and $\beta = 196$ at four instances during the first half-period. The flow is now 'antisymmetric' about the centre of the cylinder. It is seen how the surviving vortices M and N from the previous half-period form a pair that is shed and convects away at an angle of roughly 45° to the main flow direction. During the next half-period, vortices O and P will do the same towards the lower left corner as the cylinder moves in the other direction.

With four vortices being shed in each period of oscillation, the fundamental transverse force frequency is now three times the frequency of oscillation, as can be seen from the force traces depicted in figure 25. Also, a spectral analysis of the transverse force showed that the first and fifth harmonics were considerable in magnitude. Again we refer the reader to Williamson (1985) for a detail discussion of the relation between the vortex movements and the resulting forces.

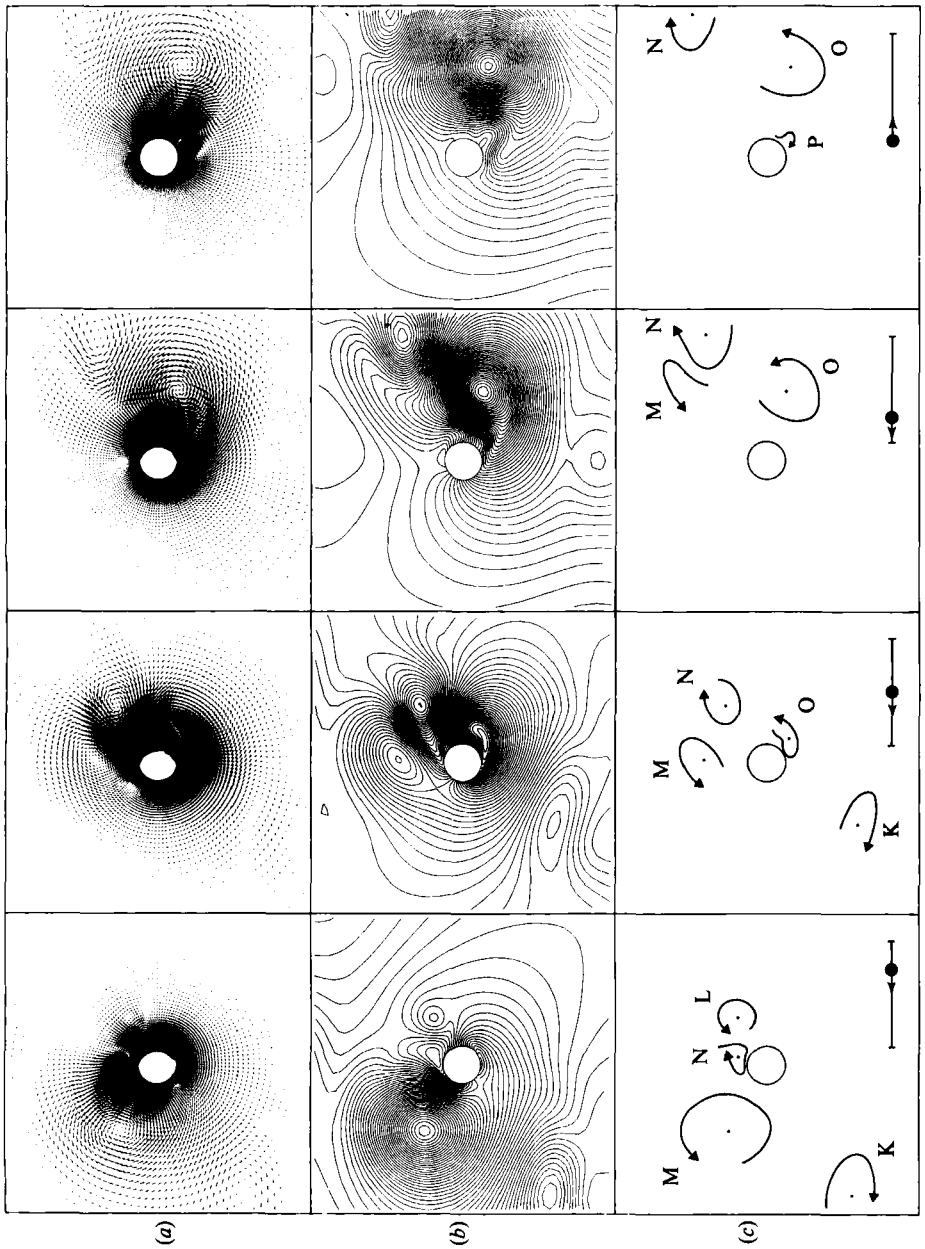

FIGURE 24. Computed flow fields for $KC = 18$ and $\beta = 196$. (*a*) Velocity vectors; the cylinder is assumed to oscillate in still water, and the frame of reference is that of the still water. (*b*) Stream-function contours, frame of reference as for (*a*), $\psi_{\min} = -6$, $\psi_{\max} = 6$ and $\Delta\psi = 0.075$. (*c*) Sketches showing the vortex patterns indicating vortex centres and direction of rotation in (*a*) and (*b*), the arrow in the lower right corner indicates the direction of the cylinder motion, and the position of the cylinder on the axis shows the time phase. Four instances from the first half-period are shown: $\frac{1}{4}\pi$, $\frac{1}{2}\pi$, $\frac{3}{4}\pi$ and π.

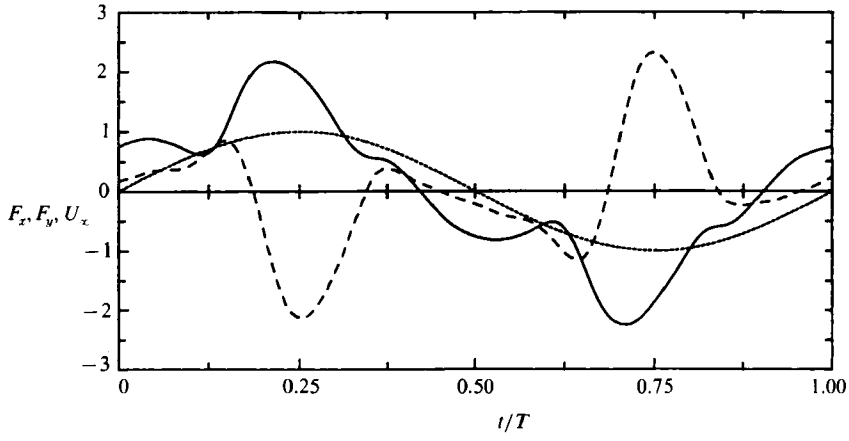

FIGURE 25. Computed force traces over one period of oscillation for $KC = 18$ and $\beta = 196$; ——, in-line force; – – –, transverse force; · · ·, external velocity.

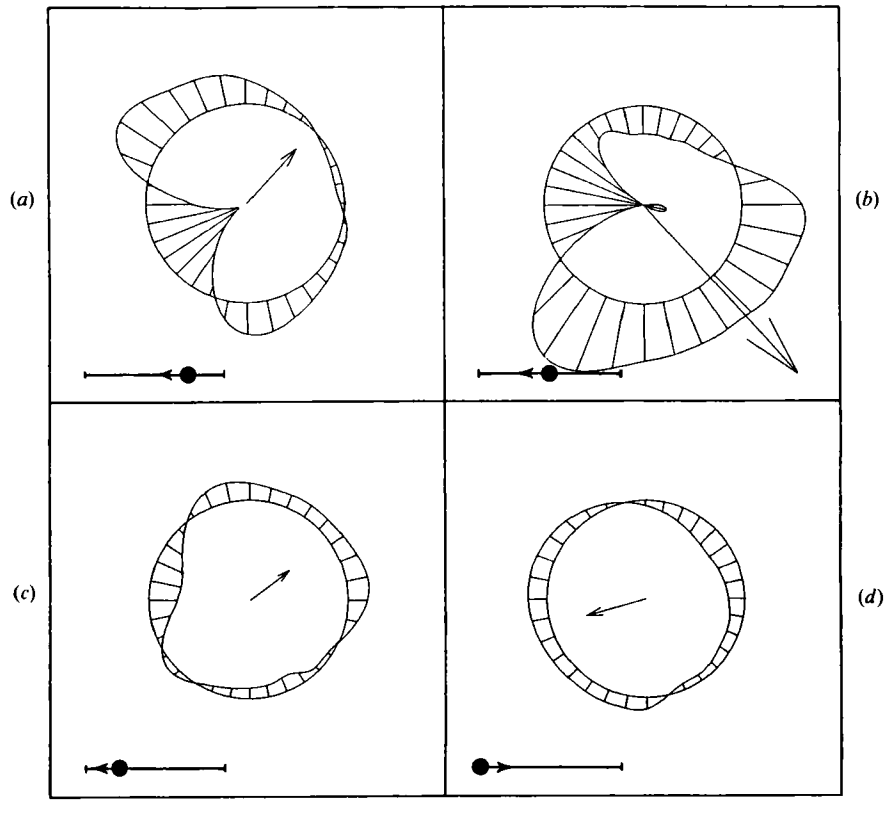

FIGURE 26. Computed surface pressure distributions for $KC = 18$ and $\beta = 196$ at the same time instances as the flow fields in figure 24. The pressure is offset such that the maximum negative pressure is equal in magnitude to the maximum positive pressure. The relative magnitude and direction of the resulting force is shown by a vector.

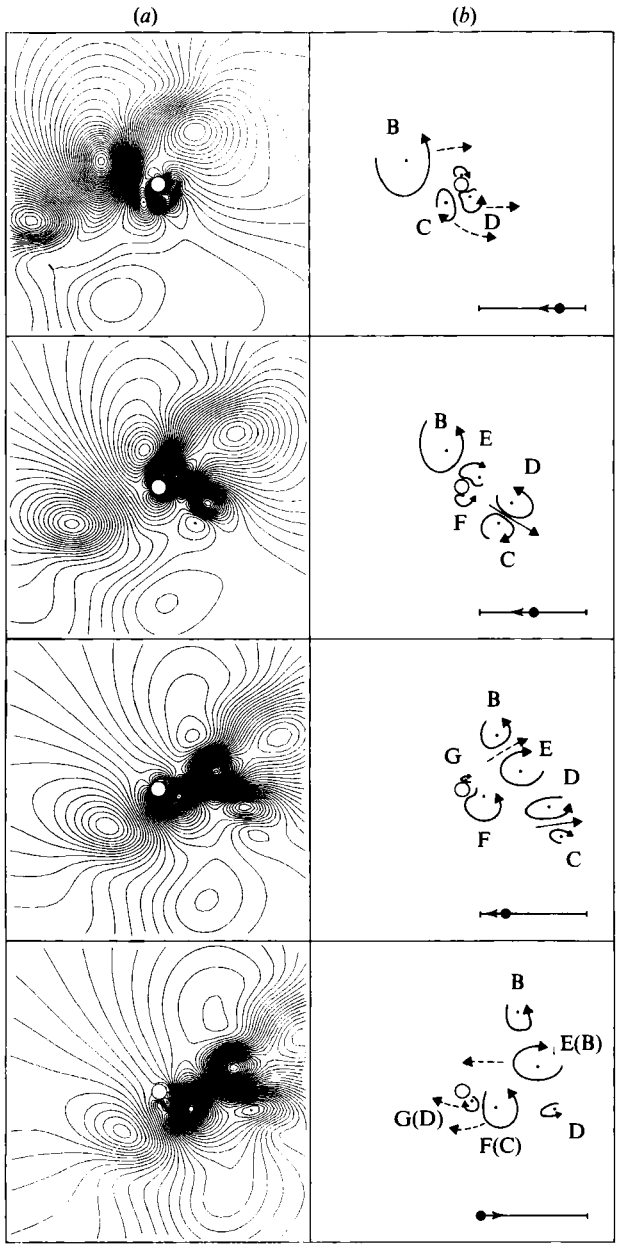

FIGURE 27. Computed flow fields for $KC = 26$ and $\beta = 196$. (*a*) Stream-function contours; the cylinder is assumed to oscillate in still water, and the frame of reference is that of the still water; $\psi_{\min} = -6$, $\psi_{\max} = 6$ and $\Delta\psi = 0.075$. (*b*) Sketches showing the vortex patterns indicating vortex centres and direction of rotation in (*a*), the arrow in the lower right corner indicates the direction of the cylinder motion, and the position of the cylinder on the axis shows the time phase. Four instances from the first half-period are shown: $\frac{1}{4}\pi$, $\frac{1}{2}\pi$, $\frac{3}{4}\pi$ and π.

Figure 26 shows the calculated distributions of surface pressure at four instances during the first half-period of oscillation. This pressure distribution is used for the force determination.

In all the calculations performed during this investigation the double-pair vortex

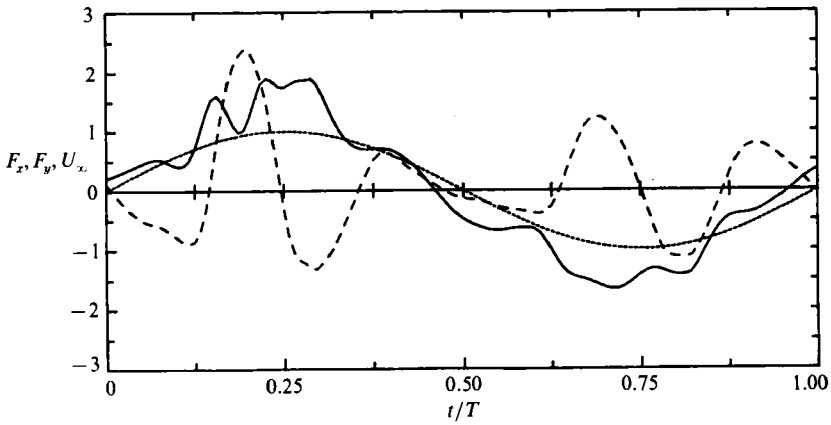

FIGURE 28. Computed force traces over one period of oscillation for $KC = 26$ and $\beta = 196$: ——, in-line force: — — —, transverse force; · · ·, external velocity.

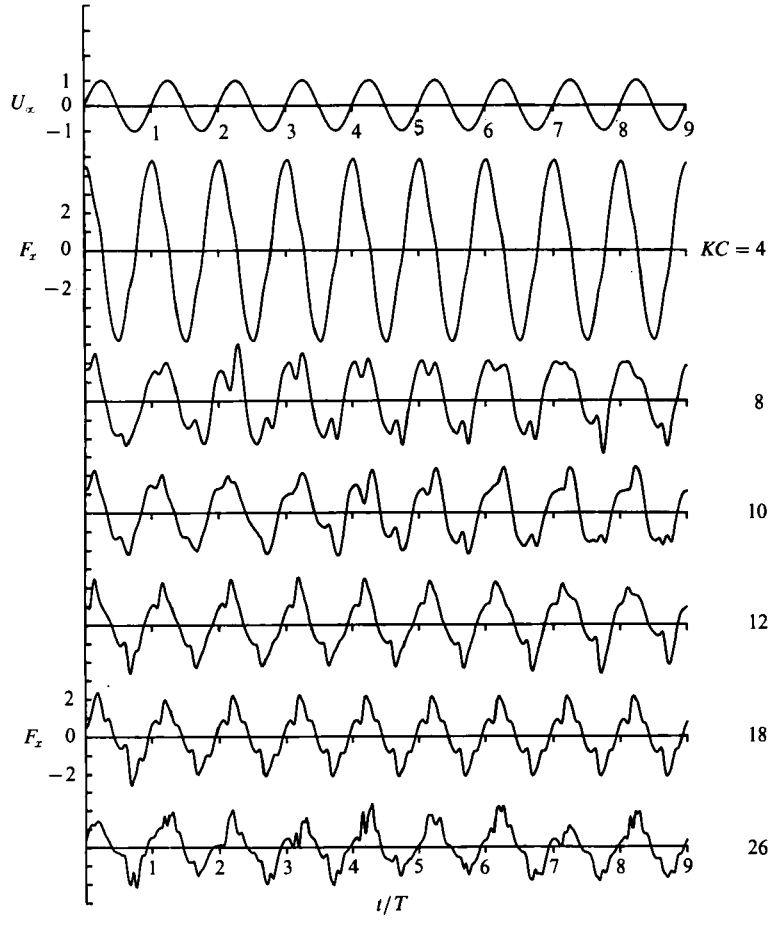

FIGURE 29. Computed in-line force traces over nine periods of oscillation at various KC-values for $\beta = 196$. The external velocity variation is depicted by the first curve. The equivalent transverse force traces may be found in figure 31.

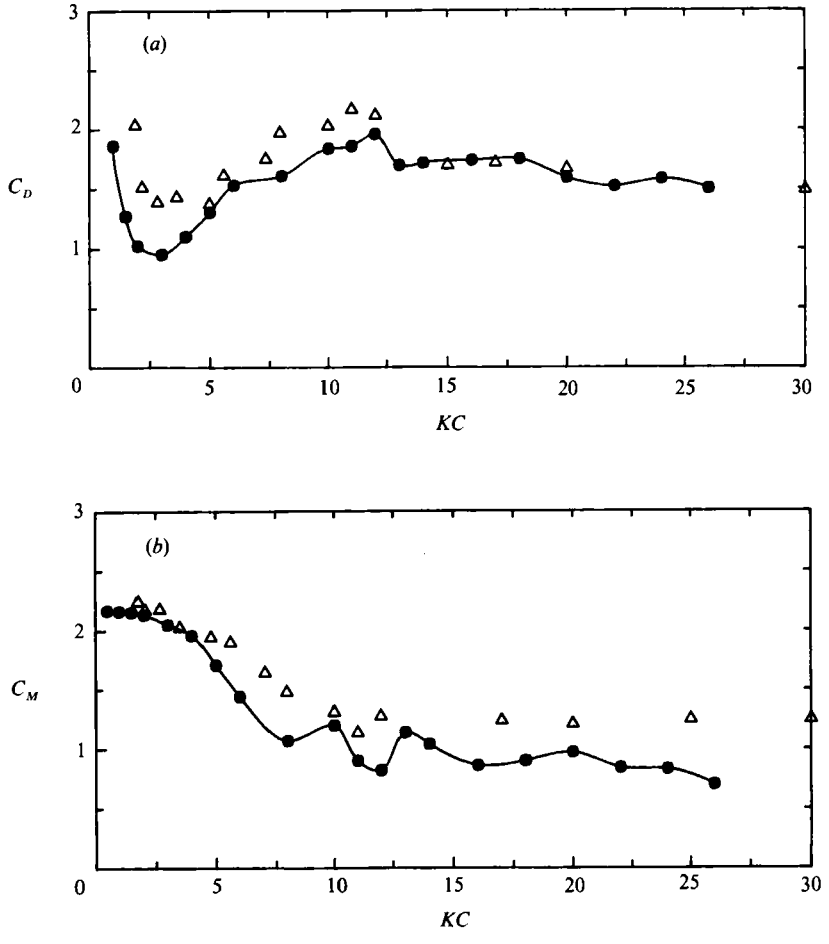

FIGURE 30. Computed in-line force coefficients for $\beta = 196$. ●, Present results; △, experiments by Obasaju *et al.* (1988). (*a*) Drag coefficient; (*b*) inertia coefficient.

pattern has been shown to be the most stable and persistent flow pattern. Once it was established in a calculation it remained. As may be seen from the transverse force traces depicted together in figure 31, the pattern was found in the interval $14 < KC < 18$, the same interval as in the various experimental investigations, almost independent of the Reynolds number in the subcritical range.

6.4.5. *Three pairs*

We have found that a transition from the double-pair regime to the 'three-pair' regime occurs for KC somewhere between 20 and 24 for $\beta = 196$. The calculated flow fields for $KC = 26$ are depicted in figure 27. Now three pairs of vortices are formed in each period of oscillation. As may be deduced from figure 28, this gives rise to a fundamental transverse force frequency of four times the frequency of oscillation.

The calculated flow pictures and force traces are in close agreement with those established in experiments (Williamson 1985; Obasaju *et al.* 1988).

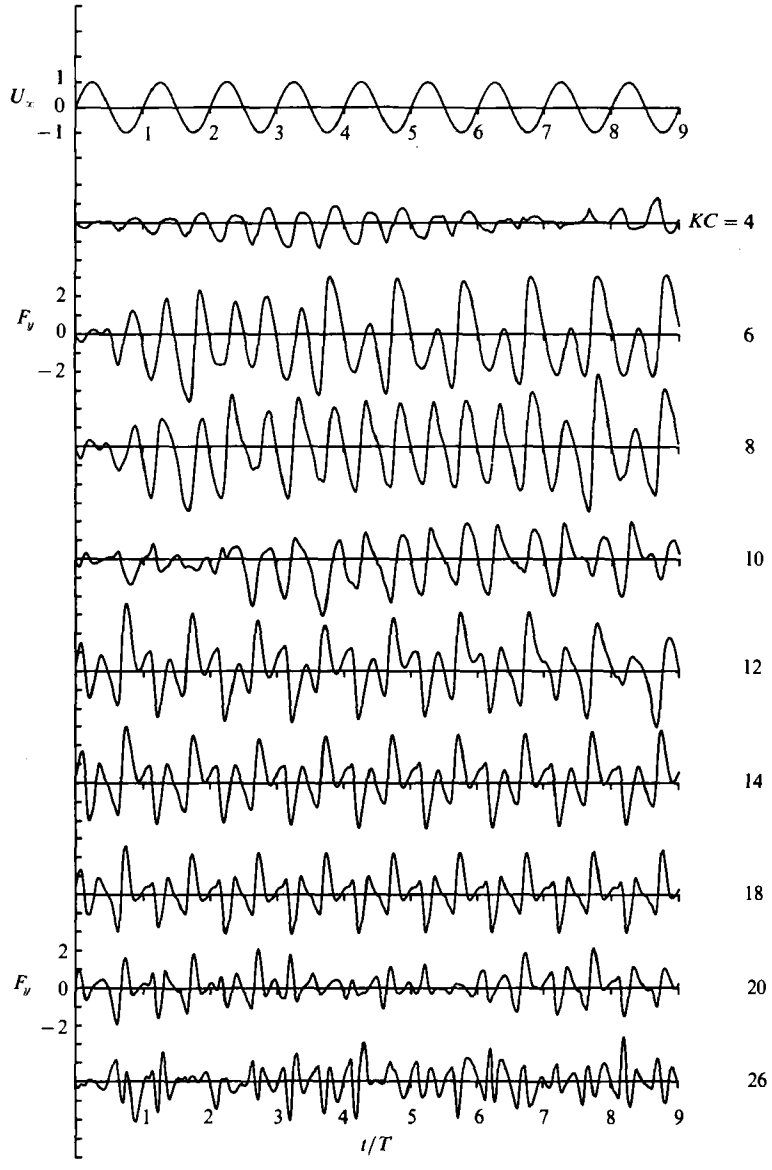

FIGURE 31. Computed transverse force traces over nine periods of oscillation at various KC-values for $\beta = 196$. The external velocity variation is depicted by the first curve. The equivalent in-line force traces may be found in figure 29.

6.5. *Force coefficients for asymmetrical flow*

To complete the presentation of the results for asymmetrical flow in the interval $4 < KC < 26$, we shall look at the calculated forces and reduce these to the conventional drag and inertia coefficients.

In figure 29 we have depicted a number of in-line force traces for different KC values, all at $\beta = 196$. These force traces have been reduced to drag and inertia coefficients as described in §6.3. The results are depicted in figure 30 together with force coefficients measured by Obasaju *et al.* (1988). A satisfactory agreement

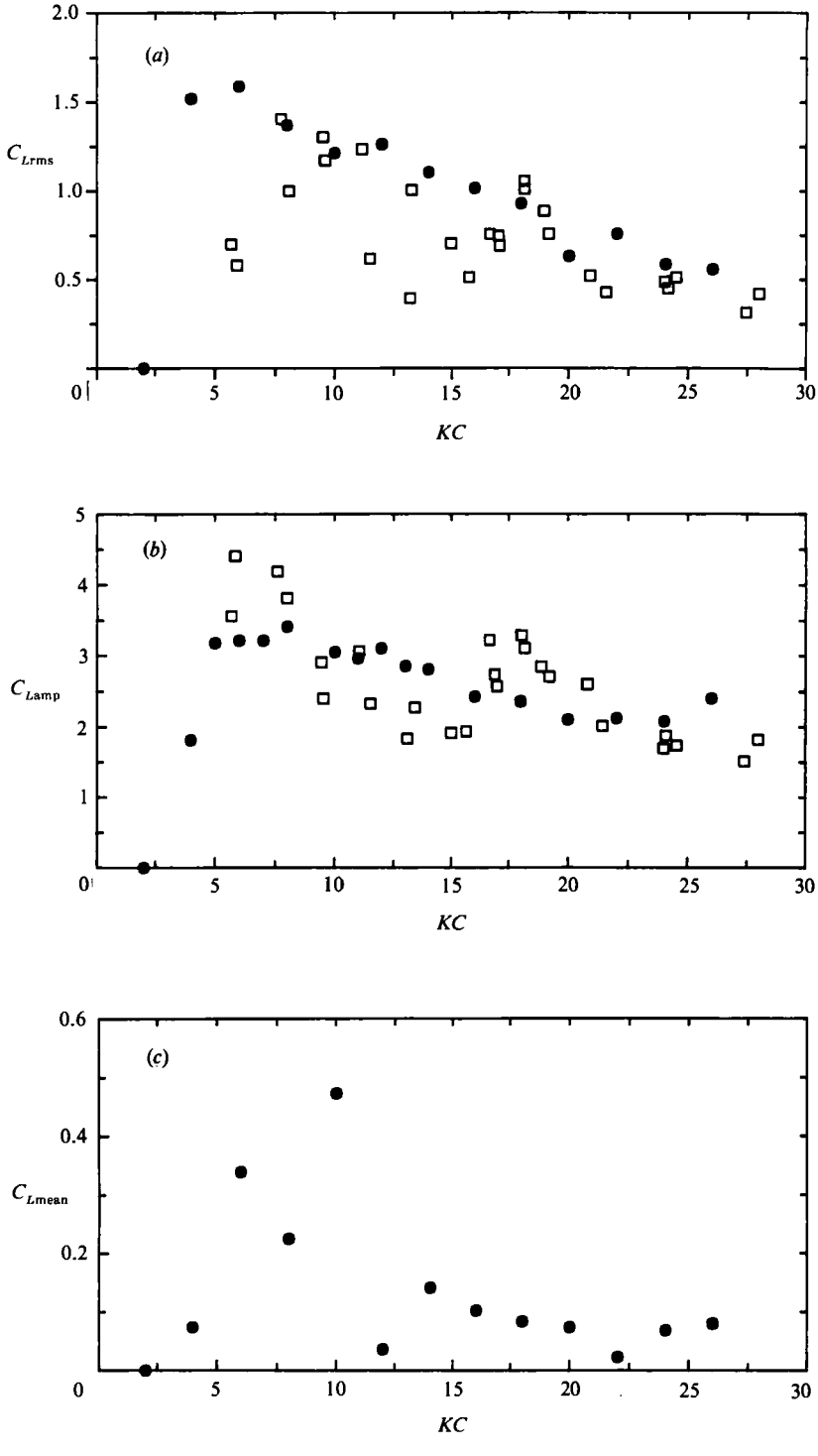

FIGURE 32. Computed transverse force coefficients for $\beta = 196$. ●, Present results; □, experiments by Maull & Milliner (1978) for $\beta = 200$. (*a*) C_{Lrms}; (*b*) C_{Lamp}; (*c*) C_{Lmean}.

between the two sets of data can be observed. It should be noted that the values for C_D and C_M are very sensitive to the flow pattern realized at a particular KC lying in a range where several flow patterns may exist. In general the increase for C_D and corresponding decrease for C_M at KC values for which a given flow pattern is dominant, and the opposite for KC values at which the flow pattern is intermittent, is well established by the computed force coefficients.

Calculated transverse force traces are depicted in figure 31, again for $\beta = 196$. Such force traces are a useful guide to the flow patterns as described above and also, for example, by Williamson (1985). In this section we shall reduce the time series to force coefficients. Figure 32 gives computed r.m.s. values, maximum values and mean values for the transverse force coefficient as a function of KC. All three coefficients are made dimensionless in the same way as F_y, cf. (24*b*). These are compared with experimental data obtained by Maull & Milliner (1978) for $\beta = 200$. As it was mentioned previously, the forces are a strong function of the prevailing vortex patterns. This is especially true for the r.m.s. lift force depicted in figure 32(*a*). Therefore the agreement with the experimental data is not convincing. The comparison is much better for the maximum transverse forces shown in figure 32(*b*). The calculated mean forces depicted in figure 32(*c*) cannot be compared with any experimental data, but the parametric variation with KC is in accordance with the observations by Williamson (1985) as well as Bearman *et al.* (1981) and Obasaju *et al.* (1988).

7. Conclusions

From the results of the numerical study of the two-dimensional oscillating flow around a circular cylinder in the range $0 < KC < 26$ we may conclude that: (i) the numerical results agree closely with the asymptotic theory by Wang (1968) as $KC \rightarrow 0$; (ii) as KC is decreased, flow separation degenerates to global flow reversal in the boundary layer due to the external pressure gradient; (iii) the inception of asymmetrical now is determined as a function of β; (iv) in the range $2 < KC < 26$, a number of flow regimes have been simulated, and the computed flow fields are in accordance with experimental data; (v) in the entire range $0 < KC < 26$ good agreement between calculated and measured forces is found.

Many of the salient features in the oscillating flow around a circular cylinder at low Reynolds number have been demonstrated in the present two-dimensional numerical computations. In order to achieve a more realistic model, however, all three dimensions must be included. Unfortunately both the present approach and the discrete vortex method cannot readily be extended to three dimensions in their present form since that would require three components of the vorticity and a vector potential.

The assistance rendered by Mr L.-C. Ekebjærg during parts of this study is gratefully acknowledged. The author benefited from discussions with Professor J. Fredsøe and Associate Professor B. Mutlu Sumer.

REFERENCES

Baba, N. & Miyata, H. 1987 Higher-order accurate difference solutions of vortex generation from a circular cylinder in an oscillatory flow. *J. Comput. Phys.* **69**, 362–396.

Bearman, P. W. 1985 Vortex trajectories in oscillatory flow. In *Proc. Intl Symp. on Separated Flow round Marine Structures, Trondheim*, pp. 133–153. Norwegian Institute of Technology, Trondheim.

BEARMAN, P. W., DOWNIE, M. J., GRAHAM, J. M. R. & OBASAJU, E. D. 1985 Forces on cylinders in viscous oscillatory flow at low Keulegan–Carpenter numbers. *J. Fluid Mech.* **154**, 337–356.

BEARMAN, P. W., GRAHAM, J. M. R., NAYLOR, P. & OBASAJU, E. E. 1981 The role of vortices in oscillatory flow about bluff bodies. In *Proc. Intl Symp. on Hydrodynamics in Ocean Engng, Trondheim, Norway, August*, pp. 621–635.

BORTHWICK, A. 1986 Comparison between two finite-difference schemes for computing the flow around a cylinder. *Intl J. Numer. Meth. Fluids* **6**, 275–290.

BOUARD, R. & COUTANCEAU, M. 1980 The early stage of development of the work behind an impulsively started cylinder for $40 < Re < 10^4$. *J. Fluid Mech.* **101**, 583–607.

BRAZA, M., CHASSAING, P. & HA MINH, H. 1986 Numerical study and physical analysis of the pressure and velocity fields in the near wake of a circular cylinder. *J. Fluid Mech.* **165**, 79–130.

GRAHAM, J. M. R. & DJAHANSOUZI, B. 1989 Hydrodynamic damping of structural elements. In *Proc. Eighth Intl Conf. Offshore Mech. and Arctic Engng, The Hague, The Netherlands*, vol. 2, pp. 289–293.

HALL, P. 1984 On the stability of unsteady boundary layer on a cylinder oscillating transversely in a viscous fluid. *J. Fluid Mech.* **146**, 347–367.

HONJI, H. 1981 Streaked flow around an oscillating circular cylinder. *J. Fluid Mech.* **107**, 509–520.

LEONARD, B. P. 1979 A survey of finite differences of opinion on numerical muddling of the incomprehensible defective confusion equation. In *Proc. ASME Winter Annual Meeting, Publ.* AMD-34.

MARTINEZ, G. 1979 Charactéristiques dynamiques et thermiques de l'ecoulement autour d'un cylindre circulaire à nombres de Reynolds moderés. Thèse docteur-Ingénieur, I.N.P. Toulouse.

MAULL, D. J. & MILLINER, M. C. 1978 Sinusoidal flow past a circular cylinder. *Coastal Engrg* **2**, 149–168.

MORISON, J. R., O'BRIEN, M. P., JOHNSON, J. W. & SCHAFF, S. A. 1950 The force exerted by surface waves on piles. *Petrol. Trans.* **189**, 149–157.

MURASHIGE, S., HINATSU, M. & KINOSHITA, T. 1989 Direct calculations of the Navier–Stokes equations for forces acting on a cylinder in oscillatory flow. In *Proc. Eighth Intl Conf. Offshore Mech. and Arctic Engng, The Hague*, vol. 2, pp. 411–418.

OBASAJU, E. D., BEARMAN, P. W. & GRAHAM, J. M. R. 1988 A study of forces, circulation and vortex patterns around a circular cylinder in oscillating flow. *J. Fluid Mech.* **196**, 467–494.

PATANKAR, S. V. 1980 *Numerical Heat Transfer and Fluid Flow.* McGraw-Hill.

ROSENHEAD, L. (ed.) 1963 *Laminar Boundary Layers.* Clarendon.

SARPKAYA, T. 1986 Forces on a circular cylinder in viscous oscillatory flow at low Keulegan–Carpenter numbers. *J. Fluid Mech.* **165**, 61–71.

SARPKAYA, T. 1989 Computational methods with vortices – The 1988 Freeman Scholar Lecture. *Trans. ASME* I: *J. Fluids Engrg* **111**, 5–52.

SKOMEDAL, N. G., VADA, T. & SORTLAND, B. 1989 Viscous forces on one and two circular cylinders in planar oscillatory flow. *Appl. Ocean Res.* **11**, 114–134.

SMITH, P. A. & STANSBY, P. K. 1988 Impulsively started flow around a circular cylinder by the vortex method. *J. Fluid Mech.* **194**, 45–77.

SORTLAND, B. 1986 Force measurements in oscillating flow on ship sections and circular cylinders in a U-tube water tank. Dr.-Ing. thesis, Norwegian Institute of Technology, Trondheim.

STANSBY, P. K. 1979 Mathematical modelling of vortex shedding from circular cylinders in planar oscillatory flows, including effects of harmonics. In *Mechanics of Wave-Induced Forces on Cylinders* (Ed. T. L. Shaw), pp. 450–460. Pitman.

STANSBY, P. K. & SMITH, P. A. 1989 Flow around a cylinder by the random vortex method. In *Proc. Eighth Intl Conf. Offshore Mech. and Arctic Eng., The Hague, The Netherlands*, vol. 2, pp. 419–426.

STOKES, G. G. 1851 On the effect of the internal friction of fluids on the motion of pendulums. *Trans. Camb. Phil. Soc.* **9**, 8–106.

TA PHUOC LOC & BOUARD, R. 1985 Numerical solution of the early stage of the unsteady viscous flow around a circular cylinder: a comparison with experimental visualization and measurements. *J. Fluid Mech.* **160**, 93–117.

VEGT, J. J. W. VAN DER & BOOM, W. C. DE 1985 Numerical simulation of flow round circular cylinders at high Reynolds numbers. In *Proc. Behaviour of Offshore Structures, Delft 1985*, pp. 227–238. Elsevier.

WANG, C.-Y. 1968 On the high-frequency oscillating viscous flows. *J. Fluid Mech.* **32**, 55–68.

WILLIAMSON, C. H. K. 1985 Sinusoidal flow relative to circular cylinders. *J. Fluid Mech.* **155**, 141–174.

WILLIAMSON, C. H. K. 1989 Oblique and parallel modes of vortex shedding in the wake of a circular cylinder at low Reynolds numbers. *J. Fluid Mech.* **206**, 579–627.